Title

Quantitative Evidence for Lanthanide-Oxygen Orbital Mixing in CeO2, PrO2, and TbO2

Journal

Journal of the American Chemical Society, 139(49)

ISSN

0002-7863

Authors

Minasian, Stefan G

Batista, Enrique R

Booth, Corwin H

et al.

Publication Date

2017-12-13

DOI

10.1021/jacs.7b10361

Peer reviewed

Quantitative evidence for lanthanide–oxygen orbital mixing in CeO_2, PrO_2, and TbO_2

Stefan G. Minasian,[1]* Enrique R. Batista,[2] Corwin H. Booth,[1] David L. Clark,[2] Jason M. Keith,[3] Stosh A. Kozimor,[2] Wayne W. Lukens,[1] Richard L. Martin,[2] David K. Shuh,[1] S. Chantal E. Stieber,[4] Tolek Tylisczcak,[1] and Xiao-dong Wen[5]

[1] *Lawrence Berkeley National Laboratory, Berkeley, CA 94720*
[2] *Los Alamos National Laboratory, Los Alamos, NM 87545*
[3] *Colgate University, Hamilton, NY 13346*
[4] *California State Polytechnic University, Pomona, CA 91768*
[5] *Chinese Academy of Sciences, Taiyuan, China*

Email: sgminasian@lbl.gov

Abstract. Understanding the nature of covalent (band-like) vs. ionic (atomic-like) electrons in metal oxides continues to be at the forefront of research in the physical sciences. In particular, the development of a coherent and quantitative model of bonding and electronic structure for the lanthanide dioxides, LnO_2 (Ln = Ce, Pr, and Tb), has remained a considerable challenge for both experiment and theory. Herein, relative changes in mixing between the O 2p orbitals and the Ln 4f and 5d orbitals in LnO_2 are evaluated quantitatively using O K-edge X-ray absorption spectroscopy (XAS) obtained with a scanning transmission X-ray microscope and density functional theory (DFT) calculations. For each LnO_2, the results reveal significant amounts of Ln 5d and O 2p mixing in the orbitals of t_{2g} (σ-bonding) and e_g (π-bonding) symmetry. The remarkable agreement between experiment and theory also shows that significant mixing with the O 2p orbitals occurs in a band derived from the 4f orbitals of a_{2u} symmetry (σ-bonding) for each compound. However, a large increase in orbital mixing is observed for PrO_2 that is ascribed to a unique interaction derived from the 4f orbitals of t_{1u} symmetry (σ- and π-bonding). O K-edge XAS and DFT results are compared with complementary L_3-edge and $M_{5,4}$-edge XAS measurements and configuration interaction calculations, which shows that each spectroscopic approach provides evidence for ground state O 2p and Ln 4f orbital mixing despite inducing very different core-hole potentials in the final state.

INTRODUCTION

Developing quantitative descriptions for chemical structure and bonding in lanthanide compounds that are grounded by both theory and experiment is a longstanding challenge in physical and inorganic chemistry.[1-12] This is especially true for the lanthanide dioxides, LnO_2 (Ln = Ce, Pr, Tb), which are the only stable dioxides formed by lanthanides, and among the only stable compounds of Pr and Tb in the +4 formal oxidation states.[13-14] A better theoretical understanding of Ln–O bonding in these materials is necessary to understand the rates and mechanisms of conversion between LnO_2 and the substoichiometric oxides, LnO_{2-x} (where $0 > x > 0.5$), via diffusion of lanthanide and oxygen ions, which features prominently in many energy-related technologies.[15-16] For example, LnO_{2-x} are employed as three-way automotive exhaust catalysts to reduce pollution owing to their reversible redox properties.[17-19] Emerging technologies also incorporate LnO_{2-x} as catalysts for steam reforming and thermochemical water splitting reactions,[20-22] and LnO_{2-x} have been used as solid-state electrolytes in fuel cells.[23-25] Considerable effort has been devoted towards improving understanding of covalency vs. electron localization in LnO_2 by employing hybrid density functional theory (DFT) calculations[26-31] in addition to X-ray spectroscopies at the L_3 ($2p_{3/2}$),[32-35] $M_{5,4}$ ($3d_{5/2,3/2}$),[36-37] and $N_{5,4}$ ($4d_{5/2,3/2}$)[37] absorption edges. Many aspects of these studies challenge the traditional viewpoints that the 4f electrons are entirely localized on the lanthanide and that bonding with the oxide ligands is best described using electrostatic models. Qualitatively, invoking a degree of covalent Ln–O bonding in LnO_2 could be justified given the growing number of synthetic,[38-46] magnetic,[47-53] spectroscopic,[54-60] and theoretical[30,61-67] studies indicating that strictly ionic models of lanthanide bonding are inadequate. For example, a new class of compounds has emerged containing lanthanide and other rare earth metals bound to oxo,[38,68-69] imido,[70-73] and carbene ligands,[74-77] among others.[78-79] Metal–ligand multiple bonding of the d-block transition metals[80-81] and actinides[82-85] is relatively well-understood, however, the extent of σ- and π-bonding involving the 4f and 5d orbitals is hard to describe precisely.[72,86] Quantitative descriptions of chemical structure and multiple bonding in prototypical compounds such as LnO_2 would help draw relationships between ground state orbital mixing and chemical reactivities and physical properties for a range of lanthanide compounds.

In recent years, X-ray absorption spectroscopy (XAS) at the ligand K-edge (1s) has emerged as one of the most versatile and direct approaches to quantitatively evaluate bonding for transition metals[87-90] and f-elements.[91-92] At the O K-edge, the approach involves quantifying the intensity of bound-state transitions between oxygen 1s orbitals and unoccupied states with oxygen 2p orbital character. Because the 1s orbitals are localized on the oxygen atoms, the intensities of the oxygen K-edge transitions are associated with the amount of O 2p character (λ) in the final state (ψ^*). Historically, efforts to quantify λ by measurement of O 1s $\rightarrow \psi^*$ transition intensities for nonconducting systems have suffered from experimental obstacles associated with the low energy of the O K-edge (*ca*. 540 eV), which magnifies errors due to surface contamination, self-absorption, and saturation. Recent work on lanthanide sesquioxides, Ln_2O_3 (Ln = La to Lu, except radioactive Pm),[54] and d-block oxyanions MO_4^{2-} (M = Cr, Mo, W) and MO_4^{1-} (Mn, Tc, Re) has shown that these issues can be minimized by obtaining O K-edge XAS in transmission mode using a scanning transmission X-ray microscope (STXM) and by using hybrid DFT calculations to develop spectral interpretations.[93-94]

Herein, a similar approach using hybrid DFT calculations and O K-edge XAS is applied to assess bonding and electronic structure in CeO_2, PrO_2, and TbO_2. The results provide evidence for a significant role of both the 4f and 5d orbitals in Ln–O bonding for each of the oxides. The O K-edge spectral features are well-resolved, which provides an opportunity to move beyond the valence formulations typically used to describe LnO_2 and form interpretations within a band structure model. This analysis reveals differences in the amount of Ln–O σ-bonding involving the 4f orbitals for each LnO_2 compound, and a unique Pr–O π-bonding interaction in PrO_2. Results are interpreted in the context of L_3-edge and $M_{5,4}$-edge X-ray spectroscopies, which – taken together – support a detailed picture of LnO_2 electronic structure involving a significant amount of O → Ln charge transfer in the ground states of CeO_2, PrO_2, and TbO_2.

RESULTS AND DISCUSSION

Lanthanide L_3- and $M_{5,4}$-edge XAS. Perhaps the most compelling spectroscopic evidence for Ln covalency has been obtained by probing excitations from the lanthanide metal core-levels using L_3- and $M_{5,4}$-edge XAS. To place the O K-edge results described below in the appropriate context, we begin by describing results from our own L_3- and $M_{5,4}$-edge XAS studies of LnO_2. The measurements also served to confirm sample purity and ensure that O K-edge results are directly comparable to those described in previous spectroscopic work cited above. Both the L_3- (2p → 5d) and $M_{5,4}$-edge (3d → 4f) spectroscopies probe electric-dipole allowed transitions from Ln core orbitals to empty or partially-occupied valence orbitals. The spectroscopic approaches can be advantageous for probing 4f orbital occupation and mixing, especially for systems with multiconfigurational ground states.[32-36,95-98] For tetravalent lanthanide oxides, multiconfigurational ground states are often described by mixing between $4f^n5d^0$ and $4f^{n+1}\underline{L}5d^0$ configurations, where n = the number of 4f electrons for a Ln^{4+} ion and $\underline{L}$ represents an O 2p hole resulting from O 2p → Ln 4f charge transfer.[32-34] Following the L_3- or $M_{5,4}$-edge measurement, spectral curve fitting and theory can be used to model changes in transition energies and intensities and to evaluate changes in O 2p → Ln 4f charge transfer between LnO_2 compounds.

Plots of the background-subtracted and normalized Ce, Pr, and Tb L_3-edge spectra together with curve-fitting models are provided in Figure 1, with the main fit parameters reported in Table 1. Each of the L_3-edges exhibits a double-peak structure that is characteristic of L_3-edge spectra obtained from other formally Ln^{4+} compounds including CeF_4, $Ce(SO_4)_2$, and $CeCl_6^{2-}$.[34,55,99] The double-peak structure has previously been attributed to transitions from the $4f^n5d^0$ and $4f^{n+1}\underline{L}5d^0$ ground states to $4f^n5d^1$ and $4f^{n+1}\underline{L}5d^1$ final states where the peak splittings (8.2(2), 8.8(2), and 7.2(1) eV observed for CeO_2, PrO_2, and TbO_2, respectively) arise from changes in the number of 4f electrons that are available to screen 5d electrons from the Ln 2p core-hole. However, the physical origin for the spectral shape has been a subject of a longstanding debate, and alternative interpretations have been proposed based on both ground- and final-state effects.[34,100-102] Within the bounds of this model, the L_3-edge peak structures were fit with pseudo-Voigt functions and a step-like function, as described more fully in the Supporting Information. The relative amount of $4f^{n+1}\underline{L}5d^0$ character in the total ground state wavefunction is

estimated from the weighted ratio of the area under the lower energy $4f^{n+1}\underline{L}5d^1$ (A_{3+}) and higher energy $4f^n5d^1$ (A_{4+}) peaks, $A_{3+}/(A_{3+} + A_{4+})$, which provides values of 56(4)%, 64(4)%, and 42(4)% for CeO_2, PrO_2, and TbO_2, respectively (Table 1). A weak shoulder feature in the lower half of the edge is roughly included in the

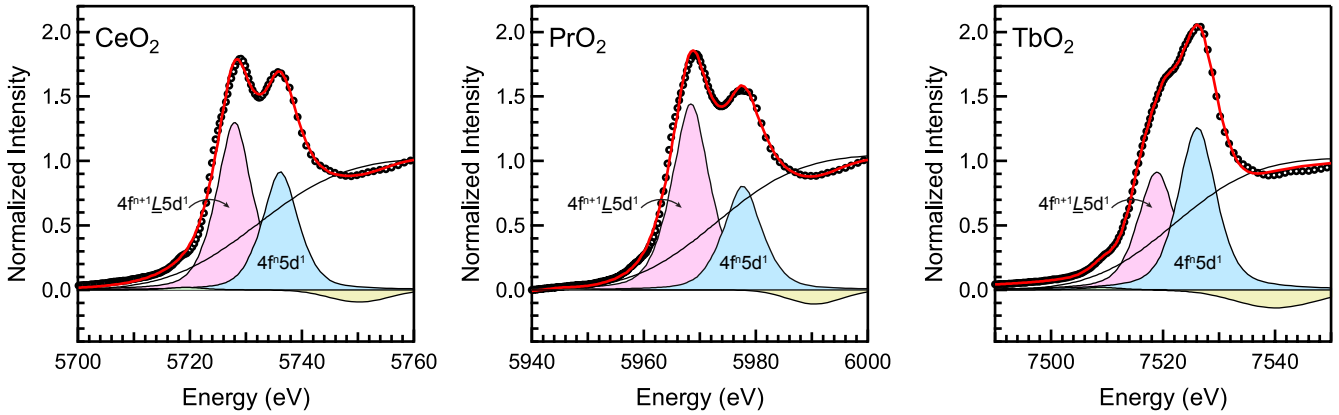

Figure 1. L_3-edge XAS experimental data (black circles) obtained for CeO_2, PrO_2, and TbO_2, and the pseudo-Voigt (green, pink, blue, and gold) and step-like functions (black) which sum to generate the curve fit (red). Shoulder features observed near the edge onset have little intensity and were modeled with a single function (green) that is barely visible from the baseline in each spectrum. A fourth function with negative amplitude (gold) accounts for the first extended x-ray absorption fine structure oscillation.

Table 1. Comparison of the main experimental Ln L_3-edge peak energies (eV) and peak areas (A_i) for LnO_2 (Ln = Ce, Pr, Tb). Reported errors are estimated from the fit assuming normally distributed errors, except for the reported error in the branching ratio, which is dominated by the estimate of the absolute error for the technique. Full fit results are provided in the Supporting Information.

	$4f^{n+1}\underline{L}5d^1$		$4f^n5d^1$		Ratio
LnO_2	eV	A_{3+}	eV	A_{4+}	$A_{3+}/(A_{3+}+A_{4+})$
CeO_2	5728.0(1)	12.5(3)	5736.2(2)	8.8(3)	0.56 ± 0.04
PrO_2	5968.4(1)	14.7(3)	5977.7(2)	8.2(2)	0.64 ± 0.04
TbO_2	7518.9(1)	9.6(2)	7526.1(1)	13.2(3)	0.42 ± 0.04

fits (Figure 1 and Table S1). It is important to note that weak and/or unresolved features, likely resulting from crystal field effects and quadrupole 2p → 4f transitions, are obscured by the main peaks in these spectra. These features are better resolved using higher resolution techniques, such as high energy-resolution fluorescence detection (HERFD).[35] Despite the limitations of the simple double-peak model described above, our approach remains reasonably accurate because the splitting of the states is on the order of the core-hole lifetime of the $2p_{3/2}$ hole.[103] Visual inspection of the spectra and branching ratios determined graphically by integration of the second-derivative spectra (see Supporting Information) provide confirmation that the branching ratio increases in the order $TbO_2 < CeO_2 \lesssim PrO_2$. Based on the spectral interpretation described above, these changes are attributed to

an increase in the amount of $4f^{n+1}\underline{L}$ character resulting from O 2p and Ln 4f orbital mixing in the ground states of CeO_2 and PrO_2 relative to TbO_2. The L_3 XAS spectra of these compounds have been studied extensively, and our values are consistent with previous results.[32-34]

The background subtracted and normalized $M_{5,4}$-edge spectra for CeO_2, PrO_2, and TbO_2 are provided in Figure 2. The $M_{5,4}$-edge spectra are split into low energy M_5 ($3d_{5/2} \rightarrow 4f_{7/2}$ and $3d_{5/2} \rightarrow 4f_{5/2}$) and high energy M_4 ($3d_{3/2} \rightarrow 4f_{5/2}$) edges due to spin-orbit coupling with the 3d core hole. Both the M_5- and M_4-edges are further split into intense main peaks and additional weaker satellite features about 5 eV higher in energy.[98-99] To quantify this effect, peaks in the experimental spectra were modeled using pseudo-Voigt functions and a step function with a 1:1 ratio of arctangent and error function contributions (Figure 2 and Table 2). The first and second derivatives of the data suggested that four pseudo-Voigt functions provided the best fit with the fewest parameters (or number of peaks) for CeO_2 and PrO_2, while additional functions were required to model the complex multiplet splitting for TbO_2. The $M_{5,4}$-edge branching ratios, defined as $A_5/(A_5 + A_4)$ – where A_5 and A_4 are the total areas under all

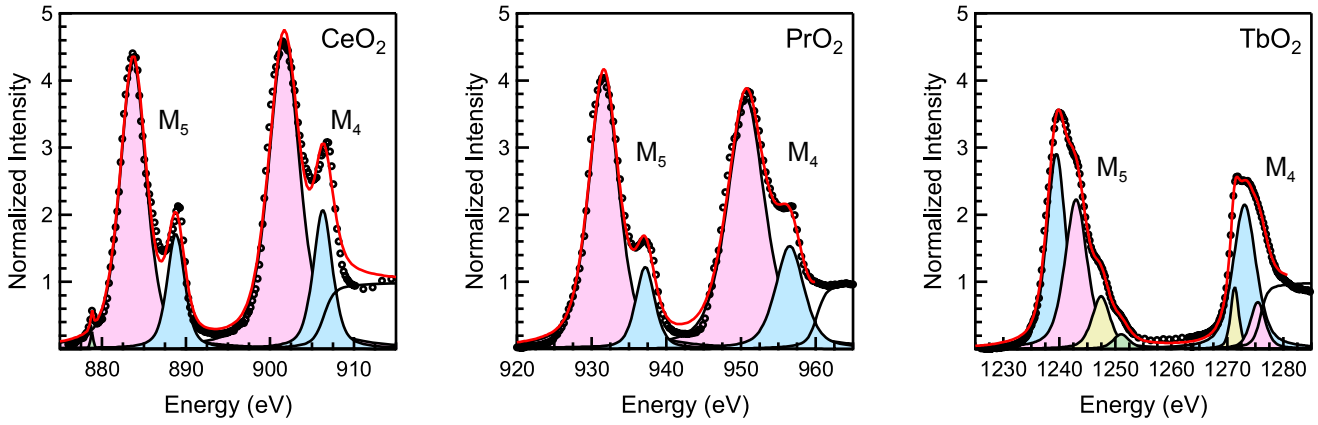

Figure 2. $M_{5,4}$-edge XAS experimental data (black circles) obtained for CeO_2, PrO_2, and TbO_2, and the pseudo-Voigt (blue and pink) and step functions (black) which sum to generate the curve fit (red). The multiplet splitting for TbO_2 was complex and modeled with additional functions (blue, pink, yellow, green)

Table 2. Comparison of experimental Ln $M_{5,4}$-edge pre-edge peak energies (eV)[a] and intensities (Int)[b] from the curve-fitting analysis for LnO_2 (Ln = Ce, Pr, Tb).

	Peak Energies (eV)				Peak Splittings (eV)		Peak Intensities (Int)				Branching
	M_5-edge		M_4-edge		Sat–Main	M_5–M_4	M_5-edge (A_5)		M_4-edge (A_4)		Ratio
LnO_2	Main	Sat	Main	Sat	Avg	Main Pks	Main	Sat	Main	Sat	$A_5/(A_5+A_4)$
CeO_2	883.7	888.8	901.7	906.3	4.8	18.0	16(2)	4.2(4)	20(2)	5.6(6)	0.44(4)
PrO_2	931.6	937.2	950.7	956.5	5.7	19.1	19(2)	3.7(4)	22(2)	7.0(7)	0.44(5)
TbO_2	1242.1		1273.2		-	31.1	26(2)		14(1)		0.65(7)

[a] The multiplet splitting for TbO_2 was complex; all functions comprising the total curve fit were used to determine the peak centroid (by weighted average) and intensity (by sum).

[b] Experimental intensities were derived from the area under pseudo-Voigt functions used to generate the curve fit and have an estimated error of less than 10%.

the functions used to model the M_5 or M_4 peaks – increased from ~0.44(5) for both CeO_2 and PrO_2 to 0.65(7) for TbO_2. Because transitions associated with the $3d^9 4f^{n+1}$ and $3d^9\underline{L}4f^{n+2}$ final states are not well-resolved in $M_{5,4}$-edge spectra (see below), these values do not directly relate to the amounts of $4f^{n+1}\underline{L}$ character in the ground states for LnO_2. However, the values are generally consistent with anticipated trends based on the number of 4f electrons for isolated atoms,[36,104-105] wherein $M_{5,4}$-edge branching ratios approach unity for later lanthanides because the $4f_{5/2}$ states are filled first and the probability of $3d_{3/2} \rightarrow 4f_{5/2}$ transitions decreases. Hence, guidance from theory was sought to understand how multiple configurations in the ground states of LnO_2 resulted in the fine structure and satellite features observed in the $M_{5,4}$-edge spectra.

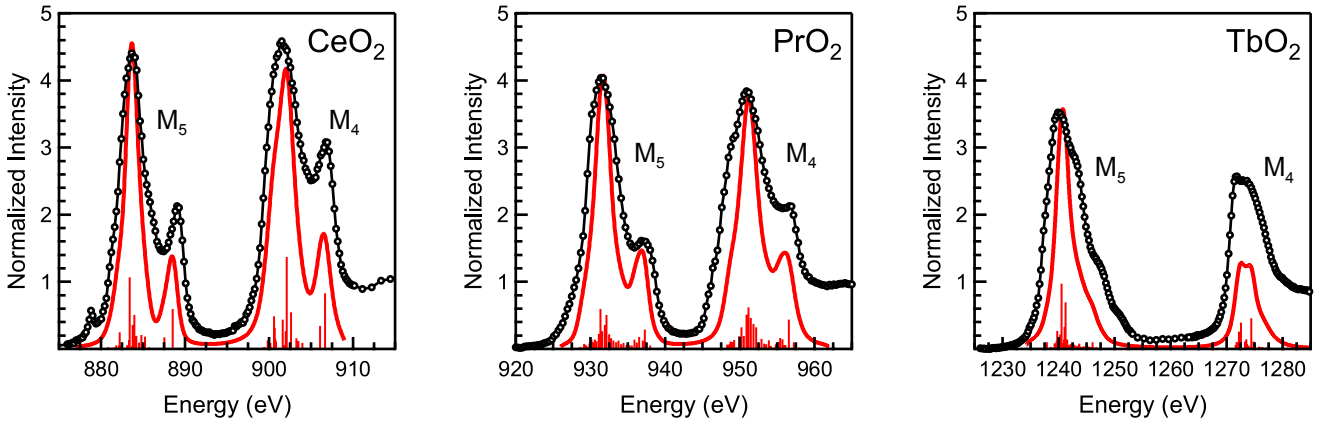

Figure 3. Comparison of the experimental (black) and the configuration interaction calculation (red) for the $M_{4,4}$-edge XAS spectra obtained for CeO_2, PrO_2, and TbO_2.

Configuration interaction (CI) calculations were conducted for LnO_2 in order to further quantify origins of spectral features and determine how ground and final state mixing between the Ln 4f and O 2p orbitals is reflected by the $M_{5,4}$-edge spectra (Figure 3). This method has been applied in a range of transition metal and lanthanide systems using the CTM4XAS program based on code by Cowan.[106-111] While CeO_2 and PrO_2 $M_{5,4}$-edge multiplets have been calculated previously,[37,109] this research adds an additional experimental handle by benchmarking computations with experimental UV-vis (ligand to metal charge transfer, LMCT) data. For both CeO_2 and PrO_2, a simple atomic model of +3 or +4 oxidation states is not in good agreement with experimental $M_{5,4}$-edge data and the higher energy satellites are not modeled accurately. Much better agreement with experimental data is reached by employing a charge transfer model that accounted for two ground state (GS) configurations, $3d^{10}4f^n$ and $3d^{10}\underline{L}4f^{n+1}$, and two final state (FS) configurations, $3d^9 4f^{n+1}$ and $3d^9\underline{L}4f^{n+2}$. Both ground and final state

configurations are additionally defined by the difference in charge transfer energy (ΔE), and the effective hopping integral (T), which is constant for all configurations. Finally, the configurations are defined by spin-orbit coupling (SOC), 4f-4f Coulomb repulsion (F_{ff}), Coulomb 3d-4f repulsion (F_{fd}), and 3d-4f Coulomb exchange (G_{fd}).

For CeO_2, the ground state is described by $3d^{10}4f^0$ and $3d^{10}\underline{L}4f^1$ configurations, and the final state is described by both $3d^9 4f^1$ and $3d^9\underline{L}4f^2$ configurations. Similarly for PrO_2, the ground state is described by the $3d^{10}4f^1$ and $3d^{10}\underline{L}4f^2$ configurations while the final state is described by $3d^9 4f^2$ and $3d^9\underline{L}4f^3$ configurations. The $M_{5,4}$-edge for CeO_2 is best modeled by ΔE_{gs} = 2.0 eV, ΔE_{fs} = -1.8 eV, and $T_{gs} = T_{fs}$ = 0.70, while the $M_{5,4}$-edge for PrO_2 is best modeled by ΔE_{gs} = 2.5 eV, ΔE_{fs} = 1.0 eV, and $T_{gs} = T_{fs}$ = 0.70. The higher energy satellites are most dependent on the value for ΔE_{fs}, suggesting that these signals are a result of final state effects. The main difference between the calculated parameters for CeO_2 vs. PrO_2 is the sign of ΔE_{fs}, however, the overall ground state descriptions are similar. For example, the calculation for CeO_2 results in a ground state that has 70% $3d^{10}4f^0$ and 30% $3d^{10}\underline{L}4f^1$ character, and provides a calculated LMCT (3.2 eV) that agrees very well with the experimental value (3.1 eV).[112] For PrO_2, the CI calculations provide a ground state that is 71% $3d^{10}4f^1$ and 29% $3d^{10}\underline{L}4f^2$ character, with a calculated LMCT of 2.2 eV (experimental = 2.4 eV).[113] These models for CeO_2 and PrO_2 model offer good agreement with both the experimental $M_{5,4}$-edge data and published UV-vis (LMCT) data. The amounts of ground state $\underline{L}4f^{n+1}$ character calculated for CeO_2 and PrO_2 (30% and 29%, respectively), are smaller than the values determined at the L_3-edge (56(4)% and 64(4)%, respectively), but provide qualitative validation of the L_3-edge interpretation described above, which also supports significant amounts of ground state Ln 4f and O 2p orbital mixing for CeO_2 and PrO_2.

In the course of this study, limitations of the CTM4XAS program prohibited incorporation of charge transfer modeling in the calculations for TbO_2. However, the $M_{5,4}$-edge spectrum for TbO_2 could be partially modeled by CI calculations in the atomic limit for Tb^{4+} that described transitions from $3d^{10}4f^7$ to $3d^9 4f^8$ final states. To most accurately model the spectrum, the 4f-4f Slater-Condon repulsion parameter was reduced to 60% of atomic values and the 4f-3d core Coulomb repulsion parameter was reduced to 90% of atomic values. Figure 3 shows that fine structure observed in the experimental $M_{5,4}$-edge is not modeled completely, particularly in the 5-10 eV region above the main M_5-edge peak. However, these high-energy features have low intensity, and otherwise the atomic limit calculations reproduce main peak positions and general aspects of the multiplet splitting. In this regard, the CI calculations provide qualitative agreement with the L_3-edge results by indicating that the $3d^{10}4f^7$ configuration (Tb^{4+}) is likely a more dominant component of the ground state for TbO_2.

Oxygen K-edge XAS. Figure 4 shows the background-subtracted and normalized O K-edge XAS obtained in transmission mode using STXM for samples of CeO_2, PrO_2 and TbO_2. Attributes of the CeO_2 O K-edge spectrum resemble earlier work,[114-115] however, to the best of our knowledge O K-edge spectra have not been reported for PrO_2 or TbO_2. Each spectrum contains several large pre-edge features in the region below 540 eV that are indicative of orbital mixing between the O 2p and lanthanide-based orbitals. For example, a broad and intense feature is observed for each LnO_2 at approximately 537 eV, along with a sharper asymmetric feature near 533 eV. At lower energies, a single additional feature is observed for CeO_2 and TbO_2 at 530.2 and 530.1 eV, respectively.

The O K-edge of PrO_2 is distinct from the other LnO_2 in that two low energy features are observed in the same low energy region, at 528.8 and 531.0 eV.

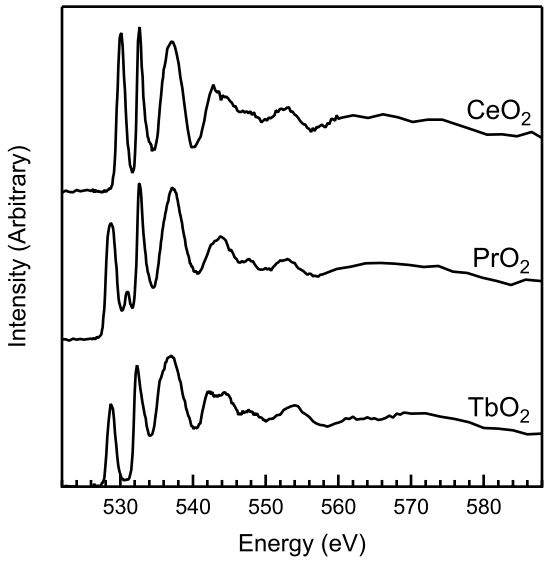

Figure 4. Oxygen K-edge XAS for particles of CeO_2, PrO_2, and TbO_2 measured in X-ray transmission mode.

A spectral curve-fit was conducted to quantify changes in peak energy and intensity throughout the LnO_2 series. The O K-edge XAS spectra were modeled as described previously using symmetrically constrained Gaussian line shapes and a step function with a 1:1 ratio of arctangent and error function contributions.[93,116] Curve-fitting models are shown in Figure 5 and summarized in Table 3. Uncertainty in the area under the Gaussian functions (hereafter referred to as the intensity) due to errors in normalization or curve-fitting were previously estimated at 10% or less based on STXM data reproducibility. For each LnO_2, the spectral fit and second derivative of the data suggest that the region above 532 eV is best modeled by three similar Gaussian functions at 532.5, 533.1, and 536.5 eV, on average. More variation in the fit model is observed at low energy, below 532 eV. For example, the spectrum of CeO_2 exhibited a single asymmetric peak that can only be modeled accurately with two Gaussian functions at 530.0 and 530.6 eV. For PrO_2, two functions at 528.3 and 528.9 eV were also required to model the asymmetric feature and a third was positioned at 531.0 eV. An effective model of the spectrum of TbO_2 was developed that included a single Gaussian function at 528.8 eV. We note that the O K-edge spectrum of TbO_2 did not return to baseline near 530.7 eV, suggesting the possible presence of additional weak transitions. However, fully unconstrained deconvolutions incorporating additional functions in this region did not converge with physically reasonable parameters, or lead to significant improvements in fit quality as determined by correlation coefficients. With these considerations and based on the DFT calculations and spectral assignments provided below, fits with additional functions for TbO_2 were rejected.

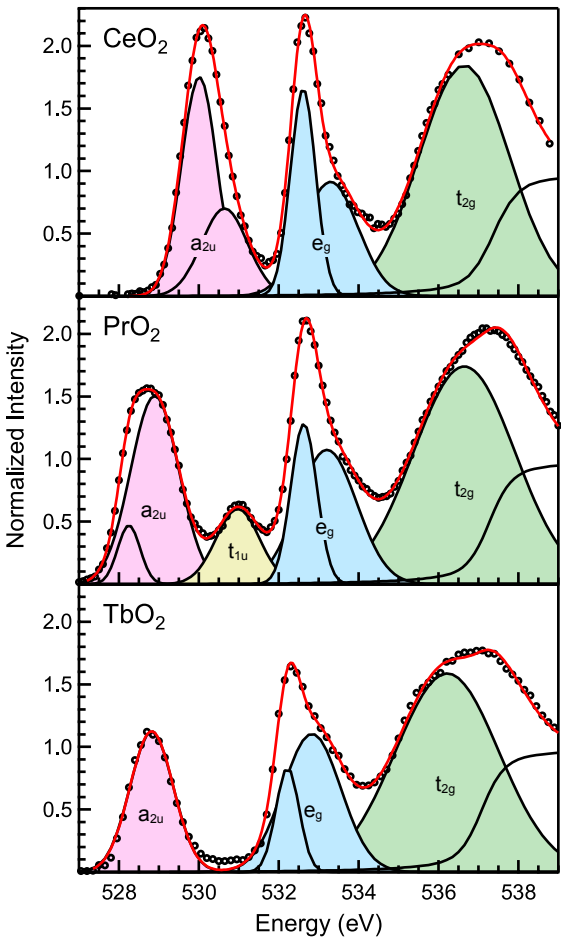

Figure 5. O K-edge XAS pre-edges (black circles), Gaussian functions (pink, yellow, blue, and green), and step functions (black traces) used to generate the total curve-fits (red traces) for LnO_2 (Ln = Ce, Pr, Tb).

Table 3. Comparison of experimental O K-edge pre-edge peak energies (eV)[a] and intensities (Int)[b] for LnO_2 (Ln = Ce, Pr, Tb). Transition assignments are given first in D_{4h} symmetry with the corresponding designations in O_h symmetry following in parentheses. Complete fit details are provided in the Supporting Information.

Transition	Energy (eV)[a]	Intensity[b]
	CeO_2	
O 1s → b_{1u} (a_{2u})	530.2	3.0(2)
O 1s → a_{1g} + b_{1g} (e_g)	533.0	2.9(2)
O 1s → b_{2g} + e_g (t_{2g})	536.6	5.2(5)
	PrO_2	
O 1s → b_{1u} (a_{2u})	528.8	2.6(2)
O 1s → e_u + a_{2u} (t_{1u})	531.0	0.8(1)
O 1s → a_{1g} + b_{1g} (e_g)	533.0	3.1(2)
O 1s → b_{2g} + e_g (t_{2g})	536.6	5.5(6)
	TbO_2	
O 1s → b_{1u} (a_{2u})	528.8	1.5(2)
O 1s → a_{1g} + b_{1g} (e_g)	532.7	2.9(2)
O 1s → b_{2g} + e_g (t_{2g})	536.2	5.2(5)

[a] The tabulated peak energies assigned to O 1s → b_{1u} (a_{2u}) and O 1s → a_{1g} + b_{1g} (e_g) transitions are determined by a weighted average of the two Gaussian functions used in the fit.

[b] Experimental intensities are derived from the area under the Gaussian functions used to generate the curve fits and have an estimated error of less than 10%.

LnO_2 Ground-State Electronic Structure Calculations. The trends in the number and energy of O K-edge transitions for LnO_2 are difficult to rationalize solely on the basis of monotonic changes in lanthanide ion size and effective nuclear charge. Hence, we turn toward DFT calculations to provide additional guidance. Recent advances in DFT including development of hybrid functionals have significantly improved descriptions of physical properties in strongly correlated materials such as CeO_2.[26] In this study, electronic structures of CeO_2, PrO_2, and TbO_2 are examined using the screened hybrid HSE functional, which has been successfully applied to many other periodic solid systems.[117-118] This approach is particularly advantageous for descriptions of 4f electron localization and electronic structure in lanthanide oxides because no localization constraints are applied to the 4f bands. Figure 6 provides the total density of states along with separate contributions from the Ln 4f, Ln 5d, and O 2p states. These calculations show that the empty or partially occupied 4f states are lower in energy than the unoccupied 5d states, and provide band gaps of 3.4, 2.3, and 1.7 eV for CeO_2, PrO_2, and TbO_2, respectively. The values are consistent with the optical band gap of CeO_2, 3.1 eV,[112] and the 2.4 eV charge transfer energy of Pr^{4+} in ThO_2.[113]

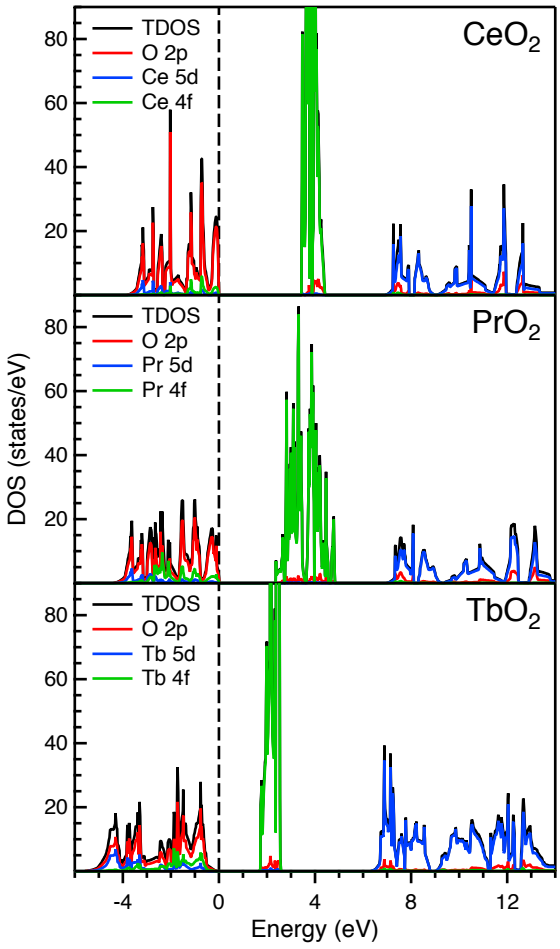

Figure 6. The calculated DOS for LnO_2 (Ln = Ce, Pr, and Tb).

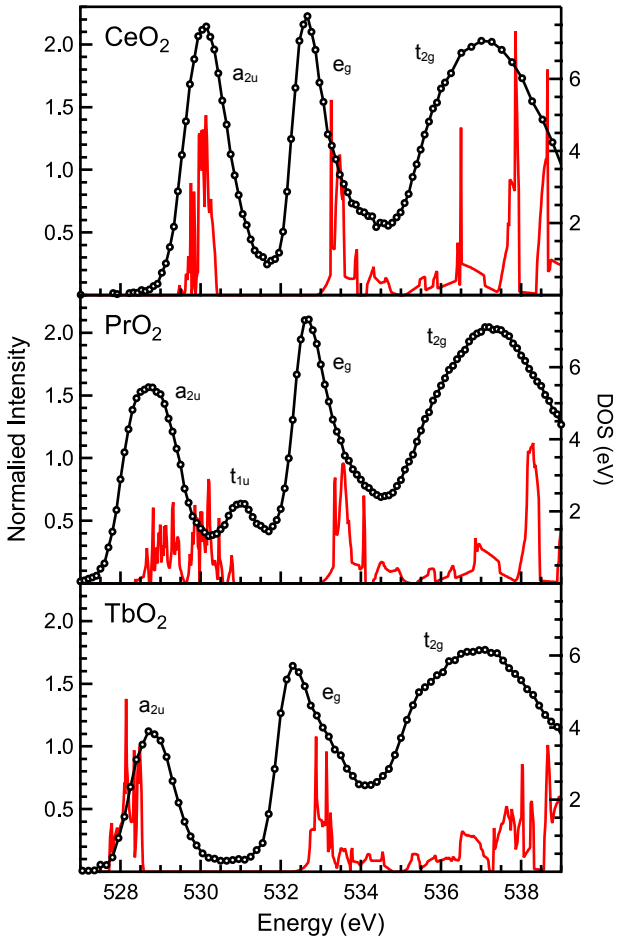

Figure 7. Experimental oxygen K-edge XAS for LnO_2 (Ln = Ce, Pr, Tb; black), the O 2p partial density of states (red) and final state assignments. Each of the O 2p PDOS plots has been shifted by 526 eV to higher energies to facilitate comparison with the experimental data.

Figure 7 demonstrates the excellent agreement with the O 2p density of states and the experimental O K-edge XAS measurements. We have shown previously that overlaying the O 2p partial DOS on the experimental O K-edge XAS spectra can guide spectral interpretations.[119] For example, Figure 7 shows that the pre-edge can be divided into two parts: a high energy region (532 to 540 eV) with transitions associated with O 2p and Ln 5d mixing, and a low energy region (below 532 eV) that arises due to O 2p and Ln 4f mixing. Previous O K-edge measurements on CeO_2 are consistent with this assignment, having ascribed the high energy peaks centered at about 533 and 536.5 eV to transitions from the O 1s to bands derived from the 5d orbitals of e_g and t_{2g} symmetry in the cubic eight-coordinate O_h geometry, and the lower-energy peak at 530 eV to transitions into bands of 4f parentage.[114] By applying these assignments we obtain splittings between the e_g and t_{2g} band centroids of 3.6 eV for all three LnO_2, which is slightly smaller than the range of e_g–t_{2g} splittings between 4 to 5 eV reported previously for OsO_2 and IrO_2.[120] In addition, the splittings of 6.4, 7.9, and 7.3 eV between the centroid of the first low energy 4f peak and the O 1s → t_{2g} transitions correlate well with reported 4f → 5d promotion energies of 6.2,

7.6, and 7.4 eV for Ce^{4+}, Pr^{4+}, and Tb^{4+}, respectively.[121] Energies for the first 4f feature (centered at 530.2, 528.8, and 528.8 eV for CeO_2, PrO_2, and TbO_2) also correlate with $Ln^{4+} \rightarrow Ln^{3+}$ reduction potentials of 1.8, 3.2, and 3.1 volts for Ce, Pr, and Tb,[122] in that the lowest unoccupied 4f orbitals decrease in energy for more oxidizing Ln^{4+} cations.

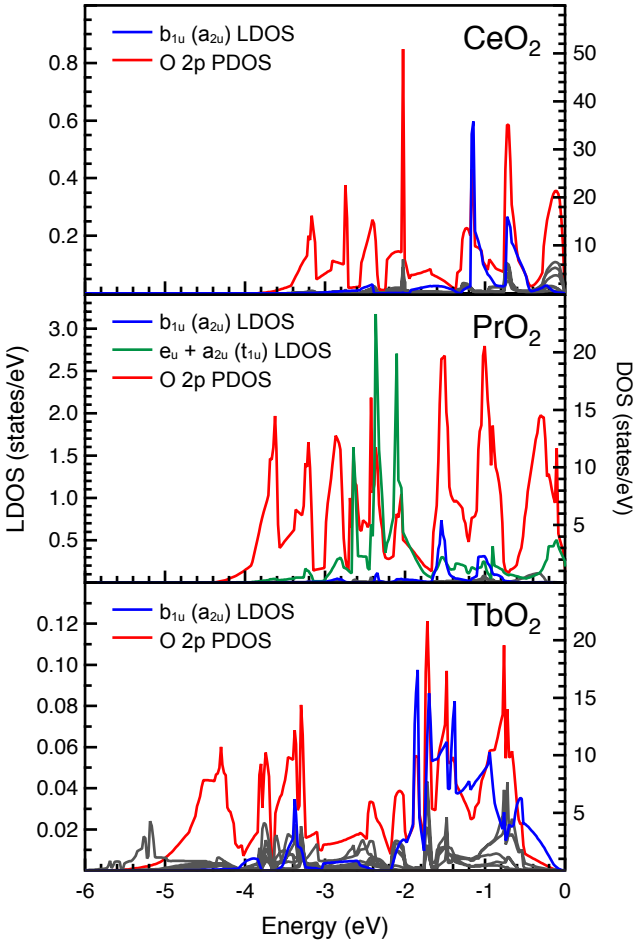

Figure 8. A plot of the O 2p partial DOS (red) and LDOS for filled 4f-derived bands (green, blue, and gray) below the Fermi level. Symmetry designations are given using D_{4h} symmetry, followed by those using idealized cubic O_h symmetry in parentheses. Significant 4f density is observed in the bonding orbitals of b_{1u} (a_{2u}) symmetry (blue) and e_u + a_{2u} (t_{1u}) symmetry (green, PrO_2 only), however, density attributable to the remaining 4f orbitals (gray) is near the baseline.

Detailed assignments for the peaks in the 4f region of the O K-edge XAS shown in Figure 7 are obtained by evaluating the local density of states (LDOS) for the occupied bands that have predominantly O 2p character (Figure 8). Expectations from group theory suggest that for O_h-symmetric LnO_2, the O 2p orbitals combine with the Ln 4f orbitals of a_{2u} (σ), t_{1u} ($\sigma + \pi$), and t_{2u} (π) symmetries (Figure 9). However, we note that the calculated structures converged with D_{4h} symmetry. For example, the LDOS for CeO_2 and TbO_2 indicates that a majority of 4f density is associated with a band derived from the singly degenerate f_{xyz} orbital of b_{1u} symmetry (a_{2u} in O_h, blue

traces), while significantly less density is associated with the remaining six 4f orbitals (gray traces). Like CeO_2 and TbO_2, the LDOS for PrO_2 also exhibits considerable density attributed to the band of b_{1u} symmetry (a_{2u} in O_h). The LDOS of PrO_2 is unique, however, because additional density is associated with four 4f orbitals at lower energy, which are attributed to a band of $e_u + a_{2u}$ symmetric orbitals (t_{1u} in O_h, green trace). Using the LDOS as a guide, the low energy features in the O K-edge XAS centered at 530.2, 528.8, and 528.8 eV for CeO_2, PrO_2, and TbO_2 are assigned to transitions from O 1s orbitals to bands derived from the 4f-orbitals of b_{1u} (a_{2u} in O_h) symmetry. The second, weaker feature at 531.0 eV for PrO_2 is attributed to a unique transition from the O 1s orbitals to bands derived from the 4f-orbitals of $e_u + a_{2u}$ (t_{1u} in O_h) symmetry, indicating that 4f orbital-derived bands are separated by 2.2 eV for PrO_2. Overall, the calculated DOS is in good agreement with the experiment, suggesting that these calculations are appropriate guides to interpret the O K-edge XAS. To simplify the remaining discussion, orbitals are described only using O_h symmetry designations.

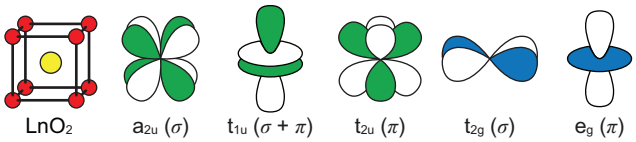

Figure 9. Representation of the lanthanide 4f and 5d orbitals in eight-coordinate O_h symmetry.

Evaluation of Ln–O bonding. The O K-edge XAS results described above show that the oxygen 2p orbitals engage in some σ- and π-bonding with the lanthanide 5d orbitals, and σ-bonding with the lanthanide 4f orbitals (for PrO_2, π-bonding with the 4f orbitals was also observed). Because pre-edge transition intensities at the O K-edge are weighted by the amount of O 2p character in the final state orbitals, they can be used to evaluate relative changes in O 2p orbital mixing as the lanthanide is changed from Ce to Pr to Tb. Beginning with transitions associated with the 5d orbitals, statistically equivalent intensities of 2.9(2), 3.1(2), and 2.9(2) are observed for the O 1s → e_g (π*) transitions for CeO_2, PrO_2, and TbO_2, respectively. The O 1s → t_{2g} (σ*) transition intensities are also equivalent for each LnO_2 (5.2(5), 5.5(6), and 5.2(5), for CeO_2, PrO_2, and TbO_2, respectively), and 1.8(2) times larger, on average, than the O 1s → e_g (π*) transitions. The relative increase in O 1s → t_{2g} (σ*) transition intensities is expected, given that greater orbital overlap for σ vs. π bonds results in covalent M–O interactions with more O 2p character. Taken together, these results suggest that O 2p mixing with the Ln 5d orbitals is a significant contributor to the covalent portion of the Ln–O bonds. Invariance in the transition intensities between LnO_2 can be rationalized given that the Ln 5d orbital energies do not vary markedly across the series, particularly when compared with the larger changes in energy for 4f orbitals as described below.[121]

For all LnO_2, the pre-edge features associated with final state orbitals of a_{2u} symmetry are evaluated using the curve-fitting analysis, with intensities of 3.0(2) and 2.6(2) for CeO_2 and PrO_2, respectively, and a much weaker peak of intensity 1.5(2) for TbO_2 (Table 3). For PrO_2, the second feature associated with the final state orbitals of t_{1u} symmetry had additional intensity of 0.8(1). Hence, the O K-edge XAS suggests that the total amount of Ln 4f

and O 2p orbital mixing generally increases in the order $TbO_2 < CeO_2 \lesssim PrO_2$, once the uncertainty associated with the measurement is considered. This trend in Ln 4f and O 2p orbital mixing is qualitatively in good agreement with the lanthanide $M_{5,4}$- and L_3-edge spectroscopic results described earlier, including the L_3-edge branching ratios. For example, both the L_3-edge XAS and $M_{5,4}$-edge XAS suggested that contribution to the ground state from the $4f^{n+1}\underline{L}5d^0$ configuration increased in the order $TbO_2 < CeO_2 \lesssim PrO_2$. The O K-edge XAS and DFT results provides new insight by showing quantitatively how multiple changes in O 2p – Ln 4f orbital mixing from TbO_2 to CeO_2 to PrO_2 occur in the orbitals of a_{2u} and t_{1u} symmetry.

These spectroscopic and theoretical results can be rationalized using first-order perturbation theory, which establishes that orbital mixing (λ) is directly related to the interaction energy (H) between the Ln 4f and O 2p orbitals and inversely proportional to their energy separation, ΔE ($E_{\text{Ln 4f}} - E_{\text{O 2p}}$).[123] For example, consider that in eight-coordinate O_h symmetry, the eight lobes of the f_{xyz} orbital are directed at the eight O atoms (Figure 9). In general, intense transitions associated with enhanced orbital mixing in the more directional a_{2u} interactions are observed for all three LnO_2 compounds as a result of a large H. With the exception of PrO_2, transitions involving the less-directional t_{1u} ($\sigma + \pi$), and t_{2u} (π) interactions are not observed due to a small H.

To understand the multiple changes in O 2p and Ln 4f orbital mixing between CeO_2, PrO_2, and TbO_2, periodic changes in both ΔE and H must be compared. Energies of the parent atomic 4f-orbitals contributing to ΔE may be roughly estimated using IE_m/m,[124] where IE_m is the ionization energy and m is the charge, which gives values of 9.0 eV for Ce, 9.6 eV for Pr, and 9.5 eV for Tb (Figure 10).[125] The potential for changes in H can be predicted from previous theoretical work,[126] which showed that the maxima for the radial charge density for the 4f electrons in Ce^{3+} (0.70 Å) and Pr^{3+} (0.67 Å) are similar (Figure 10). Meanwhile, the 4f orbital radial extension decreases significantly when moving across the series towards Tb, owing to the increased effective nuclear charge. Qualitatively, this change decreases the H term for Tb^{3+} relative to Ce^{3+} and Pr^{3+}. These periodic changes in ΔE and H show that moving from Ce^{4+} to Pr^{4+} causes a decrease of 0.6 eV in 4f orbital energies and brings them closer in energy to the O 2p orbitals of t_{1u} symmetry (decreasing ΔE), while the radial extension of the 4f orbitals decreases only slightly (similar H). As a result, the slight increase the total amount of orbital mixing is within the experimental error as one moves from CeO_2 to PrO_2. Moving from Pr^{4+} to Tb^{4+}, the average energy of the 4f orbitals changes little (similar ΔE as discussed at the start of this paragraph), while the 4f orbitals at Tb^{4+} contract significantly (decreasing H). As a result, reduced orbital mixing and weaker O 1s $\rightarrow$ a_{2u} transitions are observed for TbO_2.

This interpretation is consistent with previous DFT calculations on the actinide dioxides, AnO_2 (An = Th to Es), which showed that the 5f orbitals for later actinides are nearly degenerate with the O 2p orbitals, resulting in enhanced An–O covalency between PuO_2 and CmO_2.[118,127-128] Because the 4f orbitals for Ln^{4+} are lower in energy than the An^{4+} 5f orbitals, a near degenerate interaction is reached near the beginning of the first half of the Ln series with Ce^{4+} and Pr^{4+}, and at the beginning of the second half of the Ln series for Tb^{4+}. Figure 10 shows that the values of $IE_4/4$ for transuranic actinides Pu (8.8 eV), Am (9.3 eV), and Cm (10.0 eV) are similar to the lanthanide values provided above.[129]

Comparing O K- and Ln L_3-edge XAS. As described above, the overall increase in total Ln 4f and O 2p orbital mixing from $TbO_2 < CeO_2 \lesssim PrO_2$ established at the O K-edge is in accordance with the trend in O 2p to Ln 4f charge transfer of 42(4)% to 56(4)% to 64(4)% determined by L_3-edge measurements on TbO_2, CeO_2, and

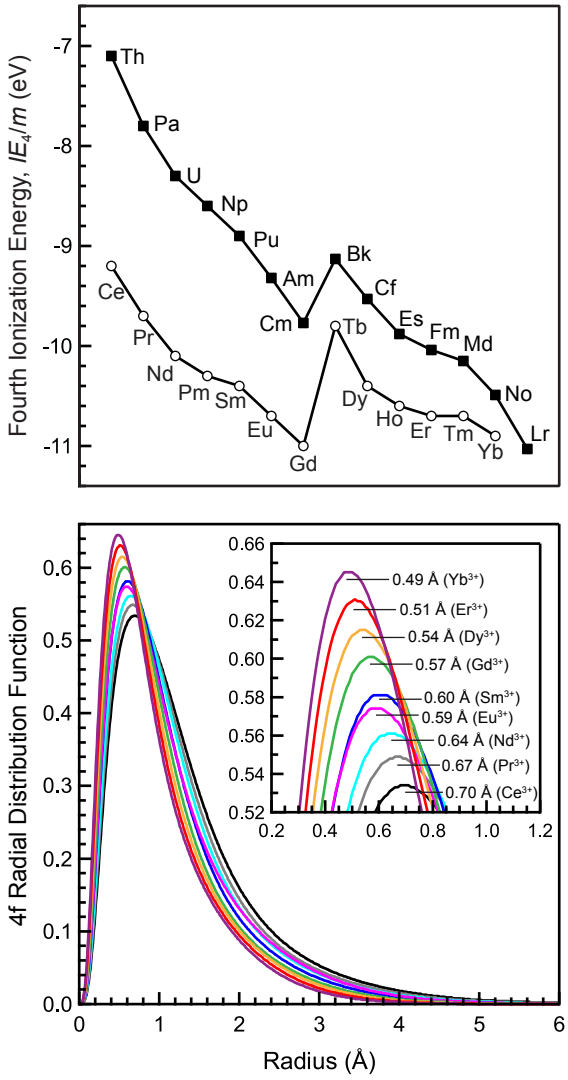

Figure 10. Rough estimates of the periodic changes in 4f orbital energy and size. Upper panel, plot of the fourth ionization energy divided by the charge ($IE_4/4$) for lanthanides[125] and actinides.[130] Lower panel, 4f orbital radial distribution functions for selected trivalent lanthanides, plotted using available data from Freeman and Watson.[126]

PrO_2, respectively. The following theoretical framework is provided to compare the L_3-edge results with the O K-edge XAS quantitatively. For LnO_2, O K-edge XAS can probe final states derived from mixing between the Ln 4f and O 2p orbitals, which can be approximated by the simple linear combination of atomic orbitals:

$$\Psi^* = N\left\{\Psi_{Ln\,4f} - \lambda\Psi_{O\,2p}\right\} \tag{1}$$

where N is a normalization constant, and λ is the coefficient of orbital mixing. As described by Solomon and coworkers,[87,131] the intensity of the O 1s → ψ^* transition increases proportionally with the square of λ:

$$I_{\mathrm{O\,1s} \rightarrow \psi^*} \cong \lambda^2 I_{\mathrm{O\,1s} \rightarrow \mathrm{O\,2p}} \tag{2}$$

where the value $I_{\mathrm{O\,1s} \rightarrow \mathrm{O\,2p}}$ is the intrinsic intensity of an O 1s → 2p transition. It is important to note that the mixing coefficient λ characterizes the amount of covalent character in the bond, as defined by Heitler and London.[132] This is easily seen if we place two electrons in the orbital and expand the wavefunction

$$\Psi^*\Psi^*\alpha\beta = \psi_{\mathrm{Ln\,4f}}\psi_{\mathrm{Ln\,4f}}\alpha\beta + \lambda\psi_{\mathrm{Ln\,4f}}\psi_{\mathrm{O2p}}(\alpha\beta\text{-}\beta\alpha) + \lambda^2\psi_{\mathrm{O2p}}\psi_{\mathrm{O2p}}\alpha\beta \tag{3}$$

such that the first and last terms are ionic components. The middle term corresponds to an electron in the 4f orbital coupled with one in the O 2p orbital to form a singlet (i.e., shared). In the many-electron, configuration interaction, "hole" representation that is often used in discussions of the L_3-edge spectra for LnO_2 compounds, this excited state wavefunction may also be represented as

$$\Psi^* = N\left\{\left|4f^n\right\rangle + \lambda\left|4f^{n+1}\underline{L}\right\rangle\right\} \tag{4}$$

Here the leading term is the usual atomic configuration with the nominal 4f orbital population based on filled O 2p orbitals (O^{2-}). The second term corresponds to a charge transfer configuration, where $\underline{L}$ represents a ligand hole created by movement of an electron from one of the oxide ligands into the Ln 4f orbitals.

Figure 11 shows the relationship between the models described by Equations 1 and 4 by comparing the O K-edge transition intensities observed for CeO_2, PrO_2 and TbO_2 to values for the amount of O 2p character (λ^2) in the antibonding orbitals determined at the L_3-edge. We note that the O K-edge spectra are normalized in the post-edge region to an intensity of 1, for one O atom; however, two oxygen atoms participate in bonding to each Ln center. Hence, values for the charge transfer observed at the Ln L_3-edge are divided by two such that $\lambda^2 = 0.28(2)$, 0.32(2), and 0.21(2) for CeO_2, PrO_2, and TbO_2, respectively. In the case of PrO_2, the intensities of both the O 1s → a_{2u} and O 1s → t_{1u} transitions are included. The plot clearly shows a correlation between the two measurements, such that the intensities of O K-edge transitions decrease to zero as values for λ^2 decrease to zero. Data for TbO_2 did not agree perfectly with this simple interpretation; as noted above, HERFD measurements would provide valuable insight regarding the effect of crystal fields when developing curve-fitting models for LnO_2. Overall, the comparison shown in Figure 10 provides support for the proposed L_3-edge peak assignments described above, and indicates that orbital mixing in the form of O 2p → Ln 4f charge transfer is an important aspect of the ground-state electronic structure for LnO_2 compounds.

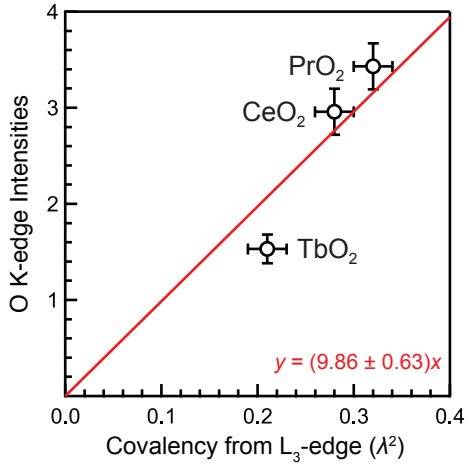

Figure 11. Graph comparing the normalized O K-edge transition intensities observed at the O K-edge to the amount of O 2p character in Ψ* due to covalency (λ^2) as a result of Ln 4f – O 2p orbital mixing for CeO_2, PrO_2, and TbO_2. The amount of covalency is taken from the L_3-edge measurements. A linear fit weighted by the experimental error and constrained to a y-intercept of zero yields a slope of 9.86 ± 0.63.

As a final note, the linear relationship between the data in Figure 11 is used to provide an estimate of 9.86 ± 0.63 for the factor $I_{\mathrm{O\,1s\rightarrow O\,2p}}$ in Equation 2, the intrinsic intensity of an O 1s → 2p transition. This value is consistent with recent measurements of the photoabsorption cross section for atomic oxygen, which gives a value for $I_{\mathrm{O\,1s\rightarrow O\,2p}}$ in the range of 10.3 ± 2.6 (calculated by normalizing the intensity of the atomic O 1s → 2p transition, 5.76 ± 1.46 Mb • eV^{-1}, to the photoionization cross section, 0.559 Mb).[133]

CONCLUSION

In summary, the O K-edge spectra of LnO_2 described above probed aspects of 4f and 5d orbital bonding selectively as they engaged in both σ- and π-type interactions with the O 2p orbitals to form metal–oxygen multiple bonds. Specifically, the O K-edge XAS and DFT calculations showed that the Ln–O bonds in CeO_2, PrO_2, and TbO_2 are comprised of multiple σ- and π-type interactions involving both the Ln 4f orbitals of a_{2u} and t_{1u} symmetry and 5d orbitals of e_g and t_{2g} symmetry. The O K-, Ln $M_{5,4}$-, and Ln L_3-edge XAS measurements also allowed for comparison of the relative role of final state effects during ligand and metal-based X-ray spectroscopies. Despite inducing very different core-hole potentials, each measurement provides evidence for Ln–O orbital mixing in the ground state. Taken together with earlier spectroscopic and theoretical studies,[26-36,96-98,134] the results strongly suggest that bonding in the lanthanide dioxides is characterized by considerable lanthanide 4f and 5d orbital mixing with the O 2p orbitals. Correlating the O K-edge XAS transition intensities to hard X-ray spectroscopies at the lanthanide L_3-edge also provided a rare opportunity to define the $I_{\mathrm{O\,1s\rightarrow O\,2p}}$ transition

dipole integral, $|\langle \psi_{O\,1s} | \boldsymbol{r} | \psi_{O\,2p} \rangle|$. We are currently exploring the generality of this result to determine whether CeO_2, PrO_2, and TbO_2 can serve as a set of intensity standards for O K-edge spectroscopies, which will enable future efforts to provide quantitative, experimentally-determined values for metal–oxygen orbital mixing in metal oxides.

EXPERIMENTAL

Synthesis. Reagents were obtained from commercial sources. PrO_2 and TbO_2 were prepared by disproportionation of Pr_6O_{11} and Tb_4O_7 in acid.[135] Prior to use, all LnO_2 powders were dried by heating to 150 °C under vacuum (10^{-3} Torr) for 24 h. Subsequent manipulations were performed with rigorous exclusion of air and moisture using Schlenk and glovebox techniques under an argon atmosphere.

Oxygen K-edge Measurements. STXM methodology was similar to that discussed previously.[93-94,136] In an argon-filled glovebox, LnO_2 powders were pulverized in a mortar and pestle, and the particles were transferred to a Si_3N_4 window (100 nm, Silson). A second window was placed over the sample to sandwich the particles, and the windows were sealed together using Hardman Double/Bubble® epoxy. Single-energy images and O K-edge XAS spectra were acquired using the STXM instrument at the Advanced Light Source-Molecular Environmental Science (ALS-MES) beamline 11.0.2, which is operated in topoff mode at 500 mA, in a ~0.5 atm He-filled chamber. The beamline uses photons from an elliptically polarizing undulator that delivers photons in the 90 to 2150 eV energy range to a variable-angle-included style plane-grating monochromator. The beamline energy was calibrated to a Rydberg feature in the O K-edge spectrum of CO_2 gas (538.9 eV). The maximum energy resolution (resolving power, $E/\Delta E$) was previously determined to be better than 7500,[137] which is consistent with the observed standard deviation for spectral transitions of ± 0.08 eV determined from comparison of spectral features over multiple particles and beam runs. For these measurements, the X-ray beam was focused with a 35 nm zone plate onto the sample, and the transmitted light was detected. Images at a single energy were obtained by raster-scanning the sample and collecting transmitted monochromatic light as a function of sample position. Spectra at particular regions of interest on the sample image were extracted from the "stack", which is a collection of images recorded at multiple, closely spaced photon energies across the absorption edge. Dwell times used to acquire an image at a single photon energy were 1 or 2 ms per pixel. To quantify the absorbance signal, the measured transmitted intensity (I) was converted to optical density using Beer−Lambert's law: $OD = ln(I/I_0) = \mu\rho d$, where I_0 is the incident photon flux intensity, d is the sample thickness, and μ and ρ are the mass absorption coefficient and density of the sample material, respectively. Incident beam intensity was measured through the sample-free region of the Si_3N_4 windows. Regions of particles with thicknesses exceeding ~ 200 nm or absorptions of >0.8 OD were omitted to ensure the spectra were in the linear regime of the Beer−Lambert law.[138] During the STXM experiment, samples particles of CeO_2, PrO_2, and TbO_2 were homogenous on the micron-scale and did not show signs of radiation damage following data acquisition. Spectra were collected using circularly polarized radiation and transition energies and intensities were reproduced from multiple independent particles, samples, and beam

runs.

The O K-edge STXM data were background subtracted using the *MBACK* algorithm in *MATLAB* and by setting the edge jump at 541 eV to an intensity of 1.0.[139] Fits to the O K-edges were performed using the program *IGOR 6.0* and a modified version of *EDG_FIT*.[140] Second-derivative spectra were used as guides to determine the number and position of peaks. Pre-edge and rising edge features were modeled by Gaussian line shapes and a step function. For the step function, a 1:1 ratio of arctangent and error function contributions was employed. Fits were performed over several energy ranges. The quality of each curve fit was determined by evaluating changes in the χ^2 and by inspecting the residual intensity, which is obtained by subtracting the fit from the experiment and should resemble a horizontal line at zero. The area under the pre-edge peaks (defined as the intensity) was calculated with the formula fwhm × ph × $(1/2)(\pi / \ln 2)^{1/2}$, where fwhm = full width at half maximum height (eV), ph = peak height (normalized intensity), and the value $(1/2)(\pi / \ln 2)^{1/2} \approx 1.065$ is a constant associated with the Gaussian function. Using the sample preparation methodology discussed above, the reported pre-edge intensities were reproduced with a standard deviation of less than 10%.

Lanthanide $M_{5,4}$-edge Measurements. Measurements at the Ce, Pr, and Tb $M_{5,4}$-edges were conducted using the ALS-MES beamline 11.0.2 STXM using the sample preparation and data acquisition methodology described above for the O K-edge measurements. Energy calibrations were performed at the Ne K-edge for Ne (867.3 eV). In a typical data analysis, a line was fit to the pre-edge region, and then subtracted from the experimental data to eliminate the background of the spectrum. The data were normalized by fitting a first-order polynomial to a 100 eV region of the spectrum beginning approximately +10 eV after the tail-end of the last M_4-edge peak. Derivative spectra were used as guides to determine the number and position of peaks, and edge features were modeled by pseudo-Voigt line shapes and a step function. For CeO_2 and PrO_2, the first and second derivatives of the data suggest that four pseudo-Voigt functions provided the best fit with the fewest functions. TbO_2 exhibited a more complex spectrum and required a total of seven pseudo-Voigt functions to achieve a reasonable fit. The area under the pseudo-Voigt functions (defined as the intensity) was calculated with the formula ph × fwhm × $^1/_4$ × { [π / $ln(2)$]$^{1/2}$ + π }, where ph = peak height (normalized intensity), fwhm = full-width at half maximum height (eV), and the value $^1/_4$ × { [π / $ln(2)$]$^{1/2}$ + π } ≈ 1.318 is a constant associated with the pseudo-Voigt function. Using the sample preparation methodology discussed above, the reported pre-edge intensities were reproduced with a standard deviation of less than 10%.

Lanthanide L_3-edge Measurements. A quantity of LnO_2 calculated to produce a absorption of 0.5 at the Ln L_3 edge was ground with boron nitride in an agate mortar and pestle to form a homogenous mixture, which was pressed into a 0.5 in by 0.125 in slot in an aluminum holder with Kapton tape windows. Data were obtained in transmission using nitrogen filled ion chambers at Stanford Synchrotron Radiation Lightsource (SSRL). The X-ray beam was monochromatized using a double-crystal monochromator (Si 220 crystals) with the second crystal detuned by 95 %. The data are energy calibrated such that the first derivative of the absorption is at 5723.0 eV, 5964.0 eV, and 7414.0 eV for the CeO_2, PrO_2, and TbO_2 samples, respectively.[141]

The degenerate $4f^n5d^0$ and $4f^{n+1}\underline{L}5d^0$ ground state configurations are split by the presence of the $2p_{3/2}$ core

hole into ($4f^n5d^1$ and $4f^{n+1}\underline{L}5d^1$ final states. A transfer to the continuum is associated with each of these states, but here we model that with a single, broad steplike function. Normally this would be an arctan function (derived from an integrated Lorentzian), but since there are two such functions underneath other peaks, we model this step with an integrated broad Gaussian as an approximation to two sharp Lorentzians. The Ln L_3-edge XANES data with this steplike function and then mainly with two pseudo-Voigt functions to model the $4f^n5d^1$ and $4f^{n+1}\underline{L}5d^1$ final states final state features (labeled as "peak 3+" and "peak 4+" below), in addition to one other pseudo-Voigt (labeled as "peak 1" below) to mimic a small peak thought to corresponding to a direct f transition.[58] Some older work suggests it is due to a d-band in the pre-edge region.[142] Specifically, the step is defined as:

$$\int_{-\infty}^{E} I_{edge} e^{-\frac{(e-E_0)^2}{2\sigma^2}} de\,,$$

and the pseudo-Voigt functions are defined as:

$$pV_i(E_i, \sigma_i, \Gamma, \eta) = \left[(1-\eta)e^{-\frac{(E-Ei)^2}{2{\sigma_i}^2}} + \eta \frac{\Gamma^2}{\Gamma^2 + \left(E - E_i^2\right)}\right],$$

where E is the incident energy, E_i is the peak energy, σ_i and Γ are the half-width of the Gaussian and the full width of the Lorentzian portions of the pseudo-Voigt, respectively. Note that with this normalization scheme, the total area under the pseudo-Voigt is $(1-\eta)\sqrt{2\pi}\sigma_i + \eta\Gamma\pi$. In these fits peaks 1, 3+, and 4+ use the same value of σ, that is, $\sigma_1=\sigma_2=\sigma_3$, and Γ is fixed at the core-hole lifetime of the given Ln L_3-edge.[103] The fourth peak roughly models the first negative extended x-ray absorption fine structure (EXAFS) oscillation. Peaks 1 and 4 are only included to attempt to account for their background contribution to the main peaks (peaks 3+ and 4+), but the final estimate of f_{3+} is only weakly dependent on this background. The data fits are shown in Figure 1 and the fit results are given in Tables 1 and S1.

CTM4XAS Calculations. Multiplet calculations were implemented using CTM4XAS, which is a program based on the original code by Cowan[106] and further developed by de Groot.[108,110] Effects of the crystal field are typically minimal in *f*-systems, so they were not included,[106] and a detailed summary of this method was previously described.[55] The configurations were defined by 4*f*-4*f* Coulomb repulsion (F_{ff}), Coulomb 3*d*-4*f* repulsion (F_{fd}), and spin-orbit coupling (SOC). For CeO_2, F_{ff} and SOC were kept at atomic values, while reductions from atomic values of 40% for F_{fd} and 80% for G_{fd} were implemented. For the $3d^94f^1$ configuration this resulted in values of F_{fd} = 3.2777, G_{fd} = 4.5267, and SOC = 3.7513 eV. For the $3d^9\underline{L}4f^2$ configuration this resulted in values of F_{ff} = 12.6281, F_{fd} = 2.9945, G_{fd} = 4.0587, and SOC = 7.4462 eV. The parameter space was also defined by ΔE_{gs} = 2.0 eV, ΔE_{fs} = -1.8 eV, and $T_{gs} = T_{fs}$ = 0.70. For PrO_2, F_{ff} and F_{fd} were kept at atomic values, while reductions from atomic values of 44% for G_{fd} and 97% for SOC were implemented. For the $3d^94f^2$ configuration this resulted in values of F_{ff} = 14.1001, F_{fd} = 8.5683, G_{fd} = 2.6287, and SOC = 7.8911 eV. For the

$3d^9\underline{L}4f^3$ configuration this resulted in values of F_{ff} = 13.0961, F_{fd} = 7.8893, G_{fd} = 2.3806, and SOC = 7.8950 eV. The parameter space was also defined by ΔE_{gs} = 2.5 eV, ΔE_{fs} = 1.0 eV, and $T_{gs} = T_{fs}$ = 0.70. For all calculations, a Gaussian broadening of 0.45 eV was applied to account for instrumental broadening and Lorentzian broadenings of 0.3 and 0.6 eV were applied to the M_5 and M_4 edges, respectively. For TbO_2, CI calculations were conducted in the atomic limit with G_{fd} and SOC at atomic values, a 40% reduction of F_{ff}, and a 10% reduction of F_{fd}. This resulted in values of F_{ff} = 7.598, F_{fd} = 3.610, G_{fd} = 6.184, and SOC = 13.363 eV. A Gaussian broadening of 0.25 eV, a Lorentzian broadening of 0.8 eV, and an energy shift of -6.7 eV were applied.

DFT Calculations. Ground-state electronic structure calculations were based on plane wave expansions using the computer program VASP (Vienna Ab-initio Simulation Package). Here the concept of range separation takes center stage: the interelectronic Coulomb potential is split into short range (SR) and long range (LR) components:

$$\frac{1}{r_{12}} = S_\omega(r_{12}) + L_\omega(r_{12}) = \frac{erfc(\omega r_{12})}{r_{12}} + \frac{erf(\omega r_{12})}{r_{12}}$$

where $r_{12} = |r_1 - r_2|$, *erf* is the error function and governs long-range (LR) behavior, *erfc* is its short–range (SR) complement, and ω determines the screening length, which is a parameter governing the extent of short-range interactions. The screened hybrid functional takes the form of the PBE0 hybrid at short range and the PBE semi-local GGA at long range,

$$E_{xc}^{HSE} = aE_x^{HF,SR}(\omega) + (1-a)E_x^{PBE,SR}(\omega) + E_x^{PBE,LR}(\omega) + E_c^{PBE} \qquad a = ¼$$

and can be viewed as an interpolation between these two limits, as discussed by Heyd, Scuseria, and Enzerhof (HSE).[143-144] This functional has proven very useful for studies of semiconductors and insulators,[117] particularly for the calculation of reliable band gaps.[145] In our recent work, we have computed the band gap and electronic properties for actinide dioxides AnO_2 (An= Th, Pa, U, Np, Pu, and Am) series and U_3O_8;[118,127,146-147] HSE predicts reasonable lattice constants and band gaps when comparing with experimental data. The value for the empirical screening parameter ω was chosen to reproduce PBE hybrid heats of formation in molecules with some consideration given to band gaps in solids. Values in the range of approximately 0.2-0.3 $Å^{-1}$ all give similar quality results, corresponding to a screening length of 3-5 Å. In our work, ω is defined as 0.207 $Å^{-1}$ as originally suggested by Heyd *et al.*[117]

The energy cutoff for the plane-wave basis was set to 500 eV. Scalar relativistic effects are included with the PAW-PBE potentials[148-149] available in the distributed code. The electrons in the configurations Ce $4p^6 5s^2 4f^1 5d^1 6s^2$, Pr $4p^6 5s^2 4f^3 6s^2$, Tb $4p^6 5s^2 4f^9 6s^2$ and O $2s^2 p^4$ are treated explicitly as valence electrons. The Brillouin zone was sampled by Monkhorst-Pack meshes of 5 × 5 × 5 grid for HSE calculations due to the considerable computational cost. The grid for HSE was tested at single points by expansion to a 6 × 6 × 6 grid. No significant differences were found. Convergence of the electronic degrees of freedom was met when the total

(free) energy change and the band structure energy change between two steps were both smaller than 1×10^{-5}. We relax all structural parameters (atomic position, lattice constants) using a conjugate-gradient algorithm until the Hellmann-Feynman forces are less than 0.01 eV/Å. Spin-orbital coupling (SOC) was not addressed; we note that it had little effect on the properties reported here in the lanthanide dioxide series.

ACKNOWLEDGEMENTS

This research was supported equally by the Director, Office of Science, Office of Basic Energy Sciences, Division of Chemical Sciences, Geosciences, and Biosciences (CSGB), Heavy Element Chemistry program of the U.S. Department of Energy (DOE) under contract no. DE-AC02-05CH11231 at LBNL (Minasian, Booth, Lukens, Shuh) and by the Director, Office of Science, Office of Basic Energy Sciences, Division of CSGB, Heavy Element Chemistry program of the U.S. DOE at LANL (Batista, Clark, Keith, Kozimor, Martin, Wen). Los Alamos National Laboratory is operated by Los Alamos National Security, LLC, for the National Nuclear Security Administration of U.S. Department of Energy (contract no. DE-AC52-06NA25396). S.C.E.S. acknowledges CPP College of Science, a CSUPERB New Investigator Grant, and NSF XSEDE (CHE160059). Beamline 11.0.2 at the Advanced Light Source (ALS) was supported in part by the aforementioned Division of CSGB, Condensed Phase and Interfacial Molecular Sciences program of the U.S. DOE under contract no. DE-AC02-05CH11231 at LBNL. This research used resources of the ALS, which is a U.S. DOE Office of Science User Facility under contract no. DE-AC02-05CH11231 at LBNL (Tyliszczak). Stanford Synchrotron Radiation Lightsource is supported by the U.S. Department of Energy, Office of Science, Office of Basic Energy Sciences under contract no. DE-AC02-76SF00515.

Supporting Information Available: Complete fit parameters, tables of X-ray absorption data, and additional computational details. This material is available free of charge via the Internet at http://pubs.acs.org.

REFERENCES

(1) Schmidt, S. F. M.; Koo, C.; Mereacre, V.; Park, J.; Heerrnann, D. W.; Kataev, V.; Anson, C. E.; Prodius, D.; Novitchi, G.; Klingeler, R.; Powell, A. K. *Inorg. Chem.* **2017**, *56*, 4796-4806.

(2) Goodwin, C. A. P.; Chilton, N. F.; Natrajan, L. S.; Boulon, M.-E.; Ziller, J. W.; Evans, W. J.; Mills, D. P. *Inorg. Chem.* **2017**, *56*, 5959-5970.

(3) Yin, X.; Wang, Y.; Bai, X.; Wang, Y.; Chen, L.; Xiao, C.; Diwu, J.; Du, S.; Chai, Z.; Albrecht-Schmitt, T. E.; Wang, S. *Nat. Commun.* **2017**, *8*.

(4) Lukens, W. W.; Speldrich, M.; Yang, P.; Duignan, T. J.; Autschbach, J.; Kogerler, P. *Dalton Trans.* **2016**, *45*, 11508-11521.

(5) Hu, Y.; Chen, C.-W.; Cao, H.; Makhmudov, F.; Grebenkemper, J. H.; Abdusalyamova, M. N.; Morosan, E.; Kauzlarich, S. M. *J. Am. Chem. Soc.* **2016**, *138*, 12422-12431.

(6) Boncher, W.; Dalafu, H.; Rosa, N.; Stoll, S. *Coord. Chem. Rev.* **2015**, *289*, 279-288.
(7) Hemmer, E.; Cavelius, C.; Huch, V.; Mathur, S. *Inorg. Chem.* **2015**, *54*, 6267-6280.
(8) Hudry, D.; Abeykoon, A. M. M.; Hoy, J.; Sfeir, M. Y.; Stach, E. A.; Dickerson, J. H. *Chem. Mater.* **2015**, *27*, 965-974.
(9) Lin, J.; Chai, P.; Diefenbach, K.; Shatruk, M.; Albrecht-Schmitt, T. E. *Chem. Mater.* **2014**, *26*, 2187-2194.
(10) Paudyal, D.; Pathak, A. K.; Pecharsky, V. K.; Gschneidner, K. A., Jr. *J. Phys. Condens. Matter* **2013**, *25*, 396002.
(11) Arnold, P. L.; Hollis, E.; Nichol, G. S.; Love, J. B.; Griveau, J.-C.; Caciuffo, R.; Magnani, N.; Maron, L.; Castro, L.; Yahia, A.; Odoh, S. O.; Schreckenbach, G. *J. Am. Chem. Soc.* **2013**, *135*, 3841-3854.
(12) Daly, S. R.; Kim, D. Y.; Girolami, G. S. *Inorg. Chem.* **2012**, *51*, 7050-7065.
(13) Eyring, L. In *Synthesis of Lanthanide and Actinide Compounds*; Meyer, G., Morss, L. R., Eds.; Springer Science: Dordrecht, 1991.
(14) Müller, B. G. In *Synthesis of Lanthanide and Actinide Compounds*; Meyer, G., Morss, L. R., Eds.; Springer Science: Dordrecht, 1991.
(15) Beschnitt, S.; Zacherle, T.; De Souza, R. A. *J. Phys. Chem. C* **2015**, *119*, 27307-27315.
(16) Milberg, B.; Juan, A.; Irigoyen, B. *Appl. Surf. Sci.* **2017**, *401*, 206-217.
(17) Zhang, Y. J.; Deng, J. G.; Zhang, H.; Liu, Y. X.; Dai, H. X. *Catal. Today* **2015**, *245*, 28-36.
(18) Sonstrom, P.; Birkenstock, J.; Borchert, Y.; Schilinsky, L.; Behrend, P.; Gries, K.; Muller, K.; Rosenauer, A.; Baumer, M. *Chemcatchem* **2010**, *2*, 694-704.
(19) Bernal, S.; Blanco, G.; Cauqui, M. A.; Corchado, P.; Pintado, J. M.; RodriguezIzquierdo, J. M. *Chem. Commun.* **1997**, 1545-1546.
(20) Montini, T.; Melchionna, M.; Monai, M.; Fornasiero, P. *Chem. Rev.* **2016**, *116*, 5987-6041.
(21) Naghavi, S. S.; Emery, A. A.; Hansen, H. A.; Zhou, F.; Ozolins, V.; Wolverton, C. *Nat. Commun.* **2017**, *8*.
(22) Balachandran, S.; Thirumalai, K.; Swaminathan, M. *RSC Adv.* **2014**, *4*, 27642-27653.
(23) Kharton, V. V.; Figueiredo, F. M.; Navarro, L.; Naumovich, E. N.; Kovalevsky, A. V.; Yaremchenko, A. A.; Viskup, A. P.; Carneiro, A.; Marques, F. M. B.; Frade, J. R. *J. Mat. Sci.* **2001**, *36*, 1105-1117.
(24) Imagawa, H.; Suda, A.; Yamamura, K.; Sun, S. H. *J. Phys. Chem. C* **2011**, *115*, 1740-1745.
(25) Shishkin, M.; Ziegler, T. *Phys. Chem. Chem. Phys.* **2014**, *16*, 1798-1808.
(26) Hay, P. J.; Martin, R. L.; Uddin, J.; Scuseria, G. E. *J. Chem. Phys.* **2006**, *125*, 034712.
(27) Da Silva, J. L. F.; Ganduglia-Pirovano, M. V.; Sauer, J.; Bayer, V.; Kresse, G. *Phys. Rev. B* **2007**, *75*, 045121.
(28) Andersson, D. A.; Simak, S. I.; Johansson, B.; Abrikosov, I. A.; Skorodumova, N. V. *Phys. Rev. B* **2007**, *75*, 035109.
(29) Tran, F.; Schweifer, J.; Blaha, P.; Schwarz, K.; Novak, P. *Phys. Rev. B* **2008**, *77*, 085123.
(30) Jiang, H.; Gomez-Abal, R. I.; Rinke, P.; Scheffler, M. *Phys. Rev. Lett.* **2009**, *102*, 126403.
(31) Gillen, R.; Clark, S. J.; Robertson, J. *Phys. Rev. B* **2013**, *87*, 125116.
(32) Bianconi, A.; Marcelli, A.; Dexpert, H.; Karnatak, R.; Kotani, A.; Jo, T.; Petiau, J. *Phys. Rev. B* **1987**, *35*, 806-812.
(33) Dexpert, H.; Karnatak, R. C.; Esteva, J. M.; Connerade, J. P.; Gasgnier, M.; Caro, P. E.; Albert, L. *Phys. Rev. B* **1987**, *36*, 1750-1753.
(34) Kaindl, G.; Schmiester, G.; Sampathkumaran, E. V.; Wachter, P. *Phys. Rev. B* **1988**, *38*, 10174-10177.

(35) Kotani, A.; Kvashnina, K. O.; Butorin, S. M.; Glatzel, P. *J. Electron. Spectrosc. Relat. Phenom.* **2011**, *184*, 210-215.
(36) Kaindl, G.; Kalkowski, G.; Brewer, W. D.; Perscheid, B.; Holtzberg, F. *J. Appl. Phys.* **1984**, *55*, 1910-1915.
(37) Kotani, A.; Ogasawara, H. *J. Electron. Spectrosc. Relat. Phenom.* **1992**, *60*, 257-299.
(38) Damon, P. L.; Wu, G.; Kaltsoyannis, N.; Hayton, T. W. *J. Am. Chem. Soc.* **2016**, *138*, 12743-12746.
(39) Fieser, M. E.; MacDonald, M. R.; Krull, B. T.; Bates, J. E.; Ziller, J. W.; Furche, F.; Evans, W. J. *J. Am. Chem. Soc.* **2015**, *137*, 369-382.
(40) Corbey, J. F.; Woen, D. H.; Palumbo, C. T.; Fieser, M. E.; Ziller, J. W.; Furche, F.; Evans, W. J. *Organometallics* **2015**, *34*, 3909-3921.
(41) Bogart, J. A.; Lippincott, C. A.; Carroll, P. J.; Booth, C. H.; Schelter, E. J. *Chem. Eur. J.* **2015**, *21*, 17850-17859.
(42) Edelmann, F. T. *Chem. Soc. Rev.* **2012**, *41*, 7657-7672.
(43) Oelkers, B.; Butovskii, M. V.; Kempe, R. *Chem. Eur. J.* **2012**, *18*, 13566-13579.
(44) Arnold, P. L.; Hollis, E.; White, F. J.; Magnani, N.; Caciuffo, R.; Love, J. B. *Angew. Chem. Int. Ed.* **2011**, *50*, 887-890.
(45) Schelter, E. J.; Wu, R.; Veauthier, J. M.; Bauer, E. D.; Booth, C. H.; Thomson, R. K.; Graves, C. R.; John, K. D.; Scott, B. L.; Thompson, J. D.; Morris, D. E.; Kiplinger, J. L. *Inorg. Chem.* **2010**, *49*, 1995-2007.
(46) King, W. A.; Marks, T. J.; Anderson, D. M.; Duncalf, D. J.; Cloke, F. G. N. *J. Am. Chem. Soc.* **1992**, *114*, 9221-9223.
(47) Harriman, K. L. M.; Brosmer, J. L.; Ungur, L.; Diaconescu, P. L.; Murugesu, M. *J. Am. Chem. Soc.* **2017**, *139*, 1420-1423.
(48) Pugh, T.; Chilton, N. F.; Layfield, R. A. *Angew. Chem. Int. Ed.* **2016**, *55*, 11082-11085.
(49) Yadav, M.; Mondal, A.; Mereacre, V.; Jana, S. K.; Powell, A. K.; Roesky, P. W. *Inorg. Chem.* **2015**, *54*, 7846-7856.
(50) Meihaus, K. R.; Fieser, M. E.; Corbey, J. F.; Evans, W. J.; Long, J. R. *J. Am. Chem. Soc.* **2015**, *137*, 9855-9860.
(51) Huang, W.; Le Roy, J. J.; Khan, S. I.; Ungur, L.; Murugesu, M.; Diaconescu, P. L. *Inorg. Chem.* **2015**, *54*, 2374-2382.
(52) Ungur, L.; Le Roy, J. J.; Korobkov, I.; Murugesu, M.; Chibotaru, L. F. *Angew. Chem. Int. Ed.* **2014**, *53*, 4413-4417.
(53) Demir, S.; Nippe, M.; Gonzalez, M. I.; Long, J. R. *Chem. Sci.* **2014**, *5*, 4701-4711.
(54) Altman, A. B.; Pacold, J. I.; Wang, J.; Lukens, W. W.; Minasian, S. G. *Dalton Trans.* **2016**, *45*, 9948-9961.
(55) Löeble, M. W.; Keith, J. M.; Altman, A. B.; Stieber, S. C. E.; Batista, E. R.; Boland, K. S.; Conradson, S. D.; Clark, D. L.; Pacheco, J. L.; Kozimor, S. A.; Martin, R. L.; Minasian, S. G.; Olson, A. C.; Scott, B. L.; Shuh, D. K.; Tyliszczak, T.; Wilkerson, M. P.; Zehnder, R. A. *J. Am. Chem. Soc.* **2015**, *137*, 2506-2523.
(56) Pacold, J. I.; Tatum, D. S.; Seidler, G. T.; Raymond, K. N.; Zhang, X.; Stickrath, A. B.; Mortensen, D. R. *J. Am. Chem. Soc.* **2014**, *136*, 4186-4191.
(57) Nocton, G.; Booth, C. H.; Maron, L.; Andersen, R. A. *Organometallics* **2013**, *32*, 5305-5312.
(58) Kvashnina, K. O.; Butorin, S. M.; Glatzel, P. *J. Anal. At. Spectrom.* **2011**, *26*, 1265-1272.
(59) Magnani, N.; Caciuffo, R.; Colineau, E.; Wastin, F.; Baraldi, A.; Buffagni, E.; Capelletti, R.; Carretta, S.; Mazzera, M.; Adroja, D. T.; Watanabe, M.; Nakamura, A. *Phys. Rev. B* **2009**, *79*.

(60) Booth, C. H.; Walter, M. D.; Daniel, M.; Lukens, W. W.; Andersen, R. A. *Phys. Rev. Lett.* **2005**, *95*.
(61) Silver, M. A.; Cary, S. K.; Garza, A. J.; Baumbach, R. E.; Arico, A. A.; Galmin, G. A.; Chen, K.-W.; Johnson, J. A.; Wang, J. C.; Clark, R. J.; Chemey, A.; Eaton, T. M.; Marsh, M. L.; Seidler, K.; Galley, S. S.; van de Burgt, L.; Gray, A. L.; Hobart, D. E.; Hanson, K.; Van Cleve, S. M.; Gendron, F.; Autschbach, J.; Scuseria, G. E.; Maron, L.; Speldrich, M.; Kögerler, P.; Celis-Barros, C.; Páez-Hernández, D.; Arratia-Pérez, R.; Ruf, M.; Albrecht-Schmitt, T. E. *J. Am. Chem. Soc.* **2017**, *139*, 13361-13375.
(62) Jung, J.; Atanasov, M.; Neese, F. *Inorg. Chem.* **2017**, *56*, 8802-8816.
(63) Krinsky, J. L.; Minasian, S. G.; Arnold, J. *Inorg. Chem.* **2011**, *50*, 345-357.
(64) Gong, Y.; Wang, X.; Andrews, L.; Chen, M.; Dixon, D. A. *Organometallics* **2011**, *30*, 4443-4452.
(65) Kerridge, A.; Kaltsoyannis, N. *C. R. Chim.* **2010**, *13*, 853-859.
(66) Loschen, C.; Carrasco, J.; Neyman, K. M.; Illas, F. *Phys. Rev. B* **2007**, *75*, 035115.
(67) Petit, L.; Svane, A.; Szotek, Z.; Strange, P.; Winter, H.; Temmerman, W. M. *J. Phys. Condens. Matter* **2001**, *13*, 8697-8706.
(68) So, Y.-M.; Wang, G.-C.; Li, Y.; Sung, H. H. Y.; Williams, I. D.; Lin, Z.; Leung, W.-H. *Angew. Chem. Int. Ed.* **2014**, *53*, 1626-1629.
(69) So, Y. M.; Li, Y.; Au-Yeung, K. C.; Wang, G. C.; Wong, K. L.; Sung, H. H. Y.; Arnold, P. L.; Williams, I. D.; Lin, Z. Y.; Leung, W. H. *Inorg. Chem.* **2016**, *55*, 10003-10012.
(70) Gordon, J. C.; Giesbrecht, G. R.; Clark, D. L.; Hay, P. J.; Keogh, D. W.; Poli, R.; Scott, B. L.; Watkin, J. G. *Organometallics* **2002**, *21*, 4726-4734.
(71) Schadle, D.; Meermann-Zimmermann, M.; Schadle, C.; Maichle-Mossmer, C.; Anwander, R. *Eur. J. Inorg. Chem.* **2015**, 1334-1339.
(72) Solola, L. A.; Zabula, A. V.; Dorfner, W. L.; Manor, B. C.; Carroll, P. J.; Schelter, E. J. *J. Am. Chem. Soc.* **2017**, *139*, 2435-2442.
(73) Solola, L. A.; Zabula, A. V.; Dorfner, W. L.; Manor, B. C.; Carroll, P. J.; Schelter, E. J. *J. Am. Chem. Soc.* **2016**, *138*, 6928-6931.
(74) Scott, J.; Fan, H.; Wicker, B. F.; Fout, A. R.; Baik, M.-H.; Mindiola, D. J. *J. Am. Chem. Soc.* **2008**, *130*, 14438-+.
(75) Mindiola, D. J.; Scott, J. *Nat. Chem.* **2011**, *3*, 15-17.
(76) Gregson, M.; Lu, E.; Tuna, F.; McInnes, E. J. L.; Hennig, C.; Scheinost, A. C.; McMaster, J.; Lewis, W.; Blake, A. J.; Kerridge, A.; Liddle, S. T. *Chem. Sci.* **2016**, *7*, 3286-3297.
(77) Gregson, M.; Lu, E.; Mills, D. P.; Tuna, F.; McInnes, E. J. L.; Hennig, C.; Scheinost, A. C.; McMaster, J.; Lewis, W.; Blake, A. J.; Kerridge, A.; Liddle, S. T. *Nat. Commun.* **2017**, *8*.
(78) Masuda, J. D.; Jantunen, K. C.; Ozerov, O. V.; Noonan, K. J. T.; Gates, D. P.; Scott, B. L.; Kiplinger, J. L. *J. Am. Chem. Soc.* **2008**, *130*, 2408-2409.
(79) Summerscales, O. T.; Gordon, J. C. *RSC Adv.* **2013**, *3*, 6682-6692.
(80) Hummel, P.; Winkler, J. R.; Gray, H. B. *Dalton Trans.* **2006**, 168-171.
(81) Winkler, J. R.; Gray, H. B. *Struct. Bond.* **2012**, *142*, 17-28.
(82) Denning, R. G.; Green, J. C.; Hutchings, T. E.; Dallera, C.; Tagliaferri, A.; Giarda, K.; Brookes, N. B.; Braicovich, L. *J. Chem. Phys.* **2002**, *117*, 8008-8020.
(83) Neidig, M. L.; Clark, D. L.; Martin, R. L. *Coord. Chem. Rev.* **2013**, *257*, 394.
(84) Spencer, L. P.; Yang, P.; Minasian, S. G.; Jilek, R. E.; Batista, E. R.; Boland, K. S.; Boncella, J. M.; Conradson, S. D.; Clark, D. L.; Hayton, T. W.; Kozimor, S. A.; Martin, R. L.; MacInnes, M.

M.; Olson, A. C.; Scott, B. L.; Shuh, D. K.; Wilkerson, M. P. *J. Am. Chem. Soc.* **2013**, *135*, 2279-2290.
(85) Anderson, N. H.; Xie, J.; Ray, D.; Zeller, M.; Gagliardi, L.; Bart, S. C. *Nat. Chem.* **2017**, *9*, 850-855.
(86) Levine, D. S.; Tilley, T. D.; Andersen, R. A. *Organometallics* **2017**, *36*, 80-88.
(87) Solomon, E. I.; Hedman, B.; Hodgson, K. O.; Dey, A.; Szilagyi, R. K. *Coord. Chem. Rev.* **2005**, *249*, 97-129.
(88) George, S. D.; Brant, P.; Solomon, E. I. *J. Am. Chem. Soc.* **2005**, *127*, 667-674.
(89) Neese, F.; Hedman, B.; Hodgson, K. O.; Solomon, E. I. *Inorg. Chem.* **1999**, *38*, 4854-4860.
(90) Shadle, S. E.; Hedman, B.; Hodgson, K. O.; Solomon, E. I. *J. Am. Chem. Soc.* **1995**, *117*, 2259-2272.
(91) Minasian, S. G.; Keith, J. M.; Batista, E. R.; Boland, K. S.; Clark, D. L.; Conradson, S. D.; Kozimor, S. A.; Martin, R. L.; Schwarz, D. E.; Shuh, D. H.; Wagner, G. L.; Wilkerson, M. P.; Wolfsberg, L. E.; Yang, P. *J. Am. Chem. Soc.* **2012**, *134*, 5586.
(92) Minasian, S. G.; Keith, J. M.; Batista, E. R.; Boland, K. S.; Clark, D. L.; Kozimor, S. A.; Martin, R. L.; Shuh, D. K.; Tyliszczak, T. *Chem. Sci.* **2014**, *5*, 351-359.
(93) Minasian, S. G.; Keith, J. M.; Batista, E. R.; Boland, K. S.; Bradley, J. A.; Daly, S. R.; Sokaras, D.; Kozimor, S. A.; Lukens, W. W.; Martin, R. L.; Nordlund, D.; Seidler, G. T.; Shuh, D. K.; Tyliszczak, T.; Wagner, G. L.; Weng, T. C.; Yang, P. *J. Am. Chem. Soc.* **2013**, *135*, 1864-1871.
(94) Bradley, J. A.; Yang, P.; Batista, E. R.; Boland, K. S.; Burns, C. J.; Clark, D. L.; Conradson, S. D.; Kozimor, S. A.; Martin, R. L.; Seidler, G. T.; Scott, B. L.; Shuh, D. K.; Tyliszczak, T.; Wilkerson, M. P.; Wolfsberg, L. E. *J. Am. Chem. Soc.* **2010**, *132*, 13914-13921.
(95) Gasgnier, M.; Schiffmacher, G.; Albert, L.; Caro, P. E.; Dexpert, H.; Esteva, J. M.; Blancard, C.; Karnatak, R. C. *J. Less-Common Met.* **1989**, *156*, 59-73.
(96) Kotani, A.; Kvashnina, K. O.; Butorin, S. M.; Glatzel, P. *Eur. Phys. J. B* **2012**, *85*, 257.
(97) Jo, T.; Kotani, A. *Phys. Rev. B* **1988**, *38*, 830-833.
(98) Thole, B. T.; Vanderlaan, G.; Fuggle, J. C.; Sawatzky, G. A.; Karnatak, R. C.; Esteva, J. M. *Phys. Rev. B* **1985**, *32*, 5107-5118.
(99) Pham, T. A.; Altman, A. B.; Stieber, S. C. E.; Booth, C. H.; Kozimor, S. A.; Lukens, W. W.; Olive, D. T.; Tyliszczak, T.; Wang, J.; Minasian, S. G.; Raymond, K. N. *Inorg. Chem.* **2016**, *55*, 9989-10002.
(100) Kas, J. J.; Rehr, J. J.; Curtis, J. B. *Phys. Rev. B* **2016**, *94*, 035156.
(101) Kotani, A. *Mod. Phys. Lett. B* **2013**, *27*.
(102) Sham, T. K.; Gordon, R. A.; Heald, S. M. *Phys. Rev. B* **2005**, *72*, 035113.
(103) Keski-Rahkonen, O.; Krause, M. O. *At. Data Nucl. Data Tables* **1974**, *14*, 139-146.
(104) Meihaus, K. R.; Minasian, S. G.; Lukens, W. W.; Kozimor, S. A.; Shuh, D. K.; Tyliszczak, T.; Long, J. R. *J. Am. Chem. Soc.* **2014**, *136*, 6056-6068.
(105) Manoubi, T.; Colliex, C.; Rez, P. *J. Electron. Spectrosc. Relat. Phenom.* **1990**, *50*, 1-18.
(106) Cowan, R. D. *Theory of Atomic Structure and Spectra*; University of California Press, 1981.
(107) de Groot, F. *Coord. Chem. Rev.* **2005**, *249*, 31-63.
(108) de Groot, F. M. F.; Kotani, A. *Core Level Spectroscopy of Solids*; Taylor and Francis: New York, 2008.
(109) Kucheyev, S. O.; Clapsaddle, B. J.; Wang, Y. M.; van Buuren, T.; Hamza, A. V. *Phys. Rev. B* **2007**, *76*, 235420.
(110) Stavitski, E.; de Groot, F. M. F. *Micron* **2010**, *41*, 687-694.

(111) Turner, S.; Lazar, S.; Freitag, B.; Egoavil, R.; Verbeeck, J.; Put, S.; Strauven, Y.; Van Tendeloo, G. *Nanoscale* **2011**, *3*, 3385-3390.
(112) Hogarth, C. A.; Aldhhan, Z. T. *Phys. Status Solidi B* **1986**, *137*, K157-K160.
(113) Hoefdraad, H. E. *J. Inorg. Nucl. Chem.* **1975**, *37*, 1917-1921.
(114) Wu, Z. Y.; Jollet, F.; Gota, S.; Thromat, N.; Gautier-Soyer, M.; Petit, T. *J. Phys. Condens. Matter* **1999**, *11*, 7185-7194.
(115) Garvie, L. A. J.; Buseck, P. R. *J. Phys. Chem. Solids* **1999**, *60*, 1943-1947.
(116) Minasian, S. G.; Keith, J. M.; Batista, E. R.; Boland, K. S.; Kozimor, S. A.; Martin, R. L.; Shuh, D. K.; Tyliszczak, T.; Vernon, L. J. *J. Am. Chem. Soc.* **2013**, *135*, 14731-14740.
(117) Henderson, T. M.; Paier, J.; Scuseria, G. E. *Phys. Status Solidi B* **2011**, *248*, 767-774.
(118) Wen, X.-D.; Martin, R. L.; Henderson, T. M.; Scuseria, G. E. *Chem. Rev.* **2013**, *113*, 1063-1096.
(119) Wen, X.-D.; Loeble, M. W.; Batista, E. R.; Bauer, E.; Boland, K. S.; Burrell, A. K.; Conradson, S. D.; Daly, S. R.; Kozimor, S. A.; Minasian, S. G.; Martin, R. L.; McCleskey, T. M.; Scott, B. L.; Shuh, D. K.; Tyliszczak, T. *J. Electron. Spectrosc. Relat. Phenom.* **2014**, *194*, 81-87.
(120) Mattheiss, L. F. *Phys. Rev. B* **1976**, *13*, 2433-2450.
(121) Brewer, L. *J. Opt. Soc. Am.* **1971**, *61*, 1666-1682.
(122) Morss, L. R. *Chem. Rev.* **1976**, *76*, 827-841.
(123) Albright, T. A.; Burdett, J. K.; Whangbo, M. *Orbital Interactions in Chemistry*; John Wiley and Sons: New York, 1985.
(124) DeKock, R. L.; Gray, H. B. *Chemical Structure and Bonding*; University Science Books: Sausalito, 1989.
(125) Martin, W. C.; Zalubas, R.; Hagan, L. *Atomic Energy Levels – The Rare Earth Elements*, NSRDS-NBS 60; U.S. Department of Commerce: Washington, DC, 1978.
(126) Freeman, A. J.; Watson, R. E. *Phys. Rev.* **1962**, *127*, 2058-2079.
(127) Wen, X.-D.; Martin, R. L.; Scuseria, G. E.; Rudin, S. P.; Batista, E. R. *J. Phys. Chem. C* **2013**, *117*, 13122-13128.
(128) Prodan, I. D.; Scuseria, G. E.; Martin, R. L. *Phys. Rev. B* **2007**, *76*.
(129) Cao, X. Y.; Dolg, M. *Journal of Molecular Structure-Theochem* **2004**, *673*, 203-209.
(130) Cao, X. Y.; Dolg, M. *Mol. Phys.* **2003**, *101*, 961-969.
(131) Shadle, S. E.; Hedman, B.; Hodgson, K. O.; Solomon, E. I. *Inorg. Chem.* **1994**, *33*, 4235-4244.
(132) Heitler, W.; London, F. *Z. Phys.* **1927**, *44*.
(133) McLaughlin, B. M.; Ballance, C. P.; Bowen, K. P.; Gardenghi, D. J.; Stolte, W. C. *Astrophys. J. Lett.* **2013**, *771*.
(134) Hu, Z.; Kaindl, G.; Ogasawara, H.; Kotani, A.; Felner, I. *Chem. Phys. Lett.* **2000**, *325*, 241-250.
(135) Brauer, G.; Pfeiffer, B. *J. Less-Common Met.* **1963**, *5*, 171-176.
(136) Magnuson, M.; Butorin, S. M.; Werme, L.; Nordgren, J.; Ivanov, K. E.; Guo, J. H.; Shuh, D. K. *Appl. Surf. Sci.* **2006**, *252*, 5615-5618.
(137) Bluhm, H.; Andersson, K.; Araki, T.; Benzerara, K.; Brown, G. E.; Dynes, J. J.; Ghosal, S.; Gilles, M. K.; Hansen, H. C.; Hemminger, J. C.; Hitchcock, A. P.; Ketteler, G.; Kilcoyne, A. L. D.; Kneedler, E.; Lawrence, J. R.; Leppard, G. G.; Majzlan, J.; Mun, B. S.; Myneni, S. C. B.; Nilsson, A.; Ogasawara, H.; Ogletree, D. F.; Pecher, K.; Salmeron, M.; Shuh, D. K.; Tonner, B.; Tyliszczak, T.; Warwick, T.; Yoon, T. H. *J. Electron. Spectrosc. Relat. Phenom.* **2006**, *150*, 86-104.
(138) Hanhan, S.; Smith, A. M.; Obst, M.; Hitchcock, A. P. *J. Electron. Spectrosc. Relat. Phenom.* **2009**, *173*, 44-49.
(139) Weng, T. C.; Waldo, G. S.; Penner-Hahn, J. E. *J. Synchrotron Rad.* **2005**, *12*, 506-510.

(140) George, G. N., EDG_FIT, Stanford Synchrotron Radiation Laboratory, Stanford Linear Accelerator Center: Stanford, CA
(141) McMaster, W. H.; Del Grande, N. K.; Mallett, J. H.; Hubbel, J. H. *Compilation of x-ray cross sections*: Lawrence Livermore National Laboratory, 1969.
(142) Soldatov, A. V.; Ivanchenko, T. S.; Dellalonga, S.; Kotani, A.; Iwamoto, Y.; Bianconi, A. *Phys. Rev. B* **1994**, *50*, 5074-5080.
(143) Heyd, J.; Scuseria, G. E.; Ernzerhof, M. *J. Chem. Phys.* **2003**, *118*, 8207-8215.
(144) Heyd, J.; Scuseria, G. E.; Ernzerhof, M. *J. Chem. Phys.* **2006**, *124*.
(145) Heyd, J.; Peralta, J. E.; Scuseria, G. E.; Martin, R. L. *J. Chem. Phys.* **2005**, *123*.
(146) Wen, X.-D.; Martin, R. L.; Roy, L. E.; Scuseria, G. E.; Rudin, S. P.; Batista, E. R.; McCleskey, T. M.; Scott, B. L.; Bauer, E.; Joyce, J. J.; Durakiewicz, T. *J. Chem. Phys.* **2012**, *137*.
(147) Wen, X.-D.; Martin, R. L.; Scuseria, G. E.; Rudin, S. P.; Batista, E. R.; Burrell, A. K. *J. Phys. Condens. Matter* **2013**, *25*.
(148) Blochl, P. E. *Phys. Rev. B* **1994**, *50*, 17953-17979.
(149) Kresse, G.; Joubert, D. *Phys. Rev. B* **1999**, *59*, 1758-1775.

For Table of Contents only: